LAWRENCE
LIVERMORE
NATIONAL
LABORATORY

LLNL-JRNL-779580

A comparison of two- and three-dimensional single-mode reshocked Richtmyer-Meshkov instability growth

M. Latini, O. Schilling

June 26, 2019

Physica D

Disclaimer

A comparison of two- and three-dimensional single-mode reshocked Richtmyer–Meshkov instability growth

Marco Latini[a,1], Oleg Schilling[b,*]

[a]*Applied and Computational Mathematics, California Institute of Technology, Pasadena, CA 91125, USA*
[b]*Lawrence Livermore National Laboratory, Livermore, CA 94550, USA*

Abstract

The growth dynamics of two- and three-dimensional single-mode reshocked Richtmyer–Meshkov instability are compared systematically using data from high-resolution implicit large-eddy simulations of a model of the Mach 1.3 air(acetone) and sulfur hexafluoride Jacobs and Krivets [Phys. Fluids 17, 034105 (2005)] shock tube experiment. The vorticity deposition by the incident shock and the dynamics of interface evolution are examined quantitatively and qualitatively. The perturbation amplitudes from the two- and three-dimensional simulations are compared to the experimental data and to the predictions of several nonlinear instability growth models. It is shown that the perturbation amplitudes from the two- and three-dimensional simulations with matching initial Richtmyer velocity are in excellent agreement with the experimental data. In addition, the dynamics of reshock (not considered in the experiment) are described in detail, and the post-reshock mixing layer amplitude growth rate is compared to the predictions of several reshock models. It is shown that using two-dimensional simulations to understand three-dimensional dynamics is valid only at early-to-intermediate times before reshock; at intermediate-to-late times after reshock the three-dimensional growth is generally larger than the corresponding two-dimensional growth. The reshock dynamics are also different between two and three dimensions. The quantitative results, together with visualizations of the flow field, were also used to contrast the difference between two- and three-dimensional vorticity and enstrophy dynamics.

Keywords: Richtmyer–Meshkov instability, reshock, nonlinear instability growth models, WENO method

1. Introduction

Richtmyer–Meshkov instability [1, 2] develops when an interface separating a heavier and a lighter material is impulsively accelerated: perturbations grow into bubbles 'penetrating' into the heavier fluid and spikes 'penetrating' into the lighter fluid, eventually developing roll-ups and complex structures through secondary shear instabilities. This instability is of fundamental interest to fluid dynamics and turbulent mixing [3–5], and for its applications to inertial confinement fusion [6], supersonic combustion [7], and astrophysics [8] (see Refs. [9, 10] for a recent review). One of the challenges in better understanding Richtmyer–Meshkov instability is the accurate modeling of the growth of the mixing layer in the nonlinear phase, as well as predicting the statistical properties and dynamics of turbulent mixing induced by this instability [11–14].

The single-mode dynamics of this instability are examined here in two and three dimensions using the formally high-order accurate weighted essentially nonoscillatory (WENO) method. The simulations are performed on a model of the Mach 1.3 reshocked Richtmyer–Meshkov instability experiment of Jacobs and Krivets [15] to both provide validation of the simulation results by comparison to experimental data, and to examine the evolution of the instability from the early linear stage, through reshock, and to late times following reshock. The WENO method is a shock-capturing method used for discretizing the compressible Euler equations of gas dynamics. As such, *ab initio* simulations are performed with a shock generated in an air(acetone) mixture interacting with a diffuse sinusoidal interface initially separating this mixture from sulfur hexafluoride.

Other numerical simulations have been performed to investigate and compare various aspects of the evolution of single- and multimode Richtmyer–Meshkov instability in two and three dimensions using a variety of numerical algorithms and methods [16–19]. Also, the predictions of the van Leer method and fifth- and ninth-order WENO methods applied to the Jacobs–Krivets experiment were compared [20], with an emphasis on the effect of grid resolution on the instability using coarse two-dimensional grids. An adaptive central-upwind sixth-order WENO method was previously used to simulate the Jacobs–Krivets experiment in two dimensions [21], with an emphasis on the differences between single- and multifluid formulations.

This paper is organized as follows. A description of the present numerical simulations, including the numerical method, initial and boundary conditions, and characterization of the vorticity deposition by the shock is given in Sec. 2. A description of the dynamics of the interface evolution is presented in Sec. 3. A comparison of the numerical amplitude to the predictions of several nonlinear instability growth models is discussed in

*Corresponding author
Email address: schilling1@llnl.gov (Oleg Schilling)
[1]Present address: Northrop Grumman Aerospace Systems, Palmdale, CA 93550, USA

Sec. 4. The dynamics of reshock are discussed in Sec. 5, including a comparison of the numerical amplitude to the predictions of several reshock models. This study is extended to three dimensions in Sec. 6. Finally, a summary of the results and conclusions is given in Sec. 7.

2. Numerical Simulations

2.1. Numerical method

The weighted essentially nonoscillatory (WENO) method is a widely used shock-capturing scheme that has previously been used in the investigation of Richtmyer–Meshkov instability [11, 12, 22, 23] and more generally of complex flows with shocks [24]. The numerical simulations of reshocked Richtmyer–Meshkov instability here were performed using the characteristic projection-based, finite-difference WENO method with ninth-order flux reconstruction [25, 26]. A methods-of-lines discretization of the compressible Euler equations is adopted.

The standard Euler equations (ρ, u_i, e, and p are the density, velocity, total energy, and pressure, respectively) are augmented by an equation for the conservation of mass fraction m of the heavier gas (the mass fraction of the lighter gas is $1 - m$):

$$\frac{\partial}{\partial t}\begin{pmatrix} \rho \\ \rho\, u_i \\ \rho\, e \\ \rho\, m \end{pmatrix} + \frac{\partial}{\partial x_j}\begin{pmatrix} \rho\, u_j \\ \rho\, u_i\, u_j + p\, \delta_{ij} \\ (\rho\, e + p)\, u_j \\ \rho\, m\, u_j \end{pmatrix} = 0 \tag{1}$$

with summation implied over repeated indices. Thus, the simulations can be interpreted as implicit large-eddy simulations (ILES) in which the inherent dissipation of the scheme provides an implicit subgrid-scale model [27, 28]. Additional details of the WENO method are provided in Appendix A.

2.2. Initial and boundary conditions

The initial and boundary conditions used for the two- and three-dimensional WENO simulations of a model of the Mach 1.3 air(acetone) and sulfur hexafluoride (SF_6) Jacobs and Krivets shock tube experiment [15] are discussed here. Jacobs and Krivets modified the vertical shock tube used in previous investigations [29, 30] to include a longer driver section, allowing a slightly stronger incident shock with Mach number $Ma_i \approx 1.3$ to be initiated. The test section had a 8.9 cm square cross section and a length of 75 cm.

A membraneless initial condition was created as follows. A mixture of air and acetone vapor, and SF_6 gas flowed towards each other, exiting from small slits located at the entrance of the test section. This generated a stable interface at the entrance of the test section. Oscillations imposed on the shock tube formed standing sinusoidal waves. This technique created a well-defined, slightly diffuse single-mode initial condition. By contrast, the use of membranes in most of the experiments performed to date gives sharp initial conditions, but the effects of the membrane fragmentation upon shock passage on the development of the instability are difficult to model numerically and are not fully understood.

Previously, using membraneless sinusoidal initial conditions and shocks with $Ma_i \approx 1.1$ and 1.2, Collins and Jacobs [30] reported excellent agreement between their experimental measurements of the amplitude growth and the prediction of the Sadot et al. [31] nonlinear growth model. However, the late-time development of the instability was limited by the arrival of the transmitted shock during the reshock phase. The larger Mach number $Ma_i \approx 1.3$ allowed the investigation of "late-time" effects, with the instability developing more rapidly for the larger Mach number. Note that there was no reshock in the experiment, but the numerical model considered here includes reshock.

Rescaling time with

$$\tau = k\, v_0\, t\,, \tag{2}$$

where the initial Richtmyer velocity is

$$v_0 = k\, a_0^-\, \Delta u\, At \tag{3}$$

with wavenumber $k = 2\pi/\lambda$, preshock amplitude a_0^-, and Atwood number $At = (\rho_{SF_6} - \rho_{air})/(\rho_{SF_6} + \rho_{air})$, the instability development attained larger values of rescaled time τ due to the larger velocity jump arising from the shock passage through the interface Δu. In addition to the $\lambda = 5.9$ cm experiment, Jacobs and Krivets also considered $\lambda = 3.6$ cm, resulting in a larger value of k, allowing the investigation of even later-time effects. Only the $\lambda = 5.9$ cm case is considered here. In a previous numerical investigation [11], upstream conditions were matched so that the adiabatic exponent corresponding to the air(acetone) mixture was used. Here, mix initial conditions are adopted (see Sec. 2.3).

The WENO simulations require the following:

1. physical properties of the gases, including the densities ρ_r (r is fluid index) and adiabatic exponent γ;
2. initial perturbation characteristics, including the preshock amplitude a_0^-, perturbation wavelength λ, and diffusion width δ_T—the single-mode initial perturbation is

   $$\eta(y) = a_0^-\, \sin(k\, y)\,, \tag{4}$$

   and the thickness function multiplying the density is an exponential filter that mitigates oscillations near discontinuities for high-order methods [32, 33]

   $$S(x,y) = \begin{cases} 1 & d \le 0 \\ \exp\left(-\alpha\, |d(x,y)|^{\,8}\right) & 0 < d < 1 \\ 0 & d \ge 1 \end{cases} \tag{5}$$

   with $d(x,y) = [x_s + \eta(y) + \delta_T - x]/(2\delta_T)$, $x_s = 3$ cm is the location of the centerline of the perturbed interface, and $\alpha = -\ln\beta$ (β is machine zero);
3. additional quantities, including the lengths of the domain L_x and L_y (and L_z in three dimensions), the shock Mach number, and the temperature ahead of the shock $T_1 = 293$ K, and;
4. numerical parameters, including the number of grid points per direction N_x and N_y (and N_z in three dimensions).

Other properties, including the initial pressure and energy are computed based on the density, temperature, and the gas constant $R_g = R_u/M$, where $R_u = 8.3143 \times 10^7$ erg/(mol K) is the universal gas constant. The pressure is then matched across the interface by adjusting the temperature of the gas T_2 [34].

The simulations were performed using the following boundary conditions:

1. free-stream at the entrance of the test section;
2. reflecting at the end of the test section, so that reshock occurs;
3. periodic in the y direction (and in the z direction for three-dimensional simulations).

The resolution of the two-dimensional simulation is summarized in Table 6, where a comparison is made to the three-dimensional simulations.

2.3. Specification of mixture properties

The physical properties of the air(acetone) are obtained using the thermodynamic properties of a mixture [35] composed of 75% air and 25% acetone vapor by volume [30], so that the density of the air(acetone) mixture is

$$\rho_{aa} = 0.75\,\rho_{air} + 0.25\,\rho_{ac}\,, \tag{6}$$

where the air mass fraction and mole fraction are

$$m_{air} = \frac{0.75\,\rho_{air}}{\rho_{aa}}\,, \quad X_{air} = \frac{m_{air}\,M_{ac}}{(1-m_{air})\,M_{air} + m_{air}\,M_{ac}}\,, \tag{7}$$

and M_r are the molecular weights. The heat capacity at constant pressure and at constant volume for the mixture are obtained by weighting the heat capacities of the components by the mass fraction: their ratio is the adiabatic exponent γ of the mixture.

Table 1 gives the properties of the air(acetone) mixture and of the SF_6 gas used in the present simulations where the adiabatic exponent corresponding to a mixture of 50% air(acetone) and 50% SF_6 by volume is adopted so that $\gamma = \gamma_1 = \gamma_2 = 1.1405$ (mix initial conditions). The simulations require only the specification of γ, and the other quantities are shown for completeness. In order to match the initial velocity, Eq. (3), of the experiment, the incident shock Mach number is slightly increased to $Ma_i = 1.313$ per shock refraction theory [34]. The postshock initial perturbation amplitude and postshock diffuse-interface width are

$$a_0^+ = \eta_c\,a_0^-\,, \quad \delta_T^+ = \eta_c\,\delta_T^-\,, \tag{8}$$

respectively, where $\eta_c \equiv 1 - \Delta u/u_{shock}$ is the compression factor [36].

Table 2 compares the flow properties as reported by Jacobs and Krivets [15] (experimental initial conditions) with the mix initial conditions. The effects of the diffuse interface can be quantified by the growth reduction factor ψ, which is a function of δ_T and At satisfying the boundary value problem [37]

$$\frac{\mathrm{d}}{\mathrm{d}x}\left(\rho\,\frac{\mathrm{d}f}{\mathrm{d}x}\right) = \left(\rho - \frac{\psi}{k\,At}\,\frac{\mathrm{d}\rho}{\mathrm{d}x}\right)k^2\,f\,, \tag{9}$$

Mix initial conditions		
	air(acetone)	SF_6
γ	1.1405	1.1405
R_g [erg/(g K)]	2.391682×10^6	5.692894×10^5
c_p [erg/(g K)]	1.941408×10^7	4.621112×10^6
c_v [erg/(g K)]	1.70224×10^7	4.051823×10^6

Table 1: The gas constant R_g, heat capacity at constant pressure c_p, and heat capacity at constant volume c_v for the air(acetone) mixture and SF_6 when $\gamma_1 = \gamma_2 = 1.1405$ for a mixture of 50% air(acetone) and 50% SF_6 by volume.

where the eigenfunction satisfies $f \to 0$ as $x \to \pm\infty$. This equation was solved numerically assuming a density profile [11]

$$\rho(y) = \rho_1 + \frac{\rho_2 - \rho_1}{2}\left[1 + \mathrm{erf}\left(\frac{\sqrt{\pi}\,y}{\delta_T}\right)\right]. \tag{10}$$

Thus, in the comparisons of the simulation amplitude data to the predictions of the nonlinear growth models discussed later, the amplitude growth rates are adjusted to account for the diffuse interface by the rescaling

$$\frac{\mathrm{d}a}{\mathrm{d}t} \longrightarrow \frac{1}{\psi}\,\frac{\mathrm{d}a}{\mathrm{d}t}\,. \tag{11}$$

Table 2 also includes the physical and numerical parameters used in the single-mode sinusoidal perturbation in two dimensions.

2.4. Baroclinic circulation deposition on the interface and comparison to the predictions of models

The circulation deposited on the interface by a shock constitutes the principal driving mechanism for the evolution of Richtmyer–Meshkov instability from an initially-perturbed interface. The misalignment of the density gradient and pressure gradient causes a deposition of vorticity $\boldsymbol{\omega} \equiv \boldsymbol{\nabla}\times\mathbf{u}$ on the interface through baroclinic vorticity production $\mathcal{P} \equiv (\boldsymbol{\nabla}\rho \times \boldsymbol{\nabla}p)/\rho^2$: in two dimensions

$$\frac{\mathrm{d}\boldsymbol{\omega}}{\mathrm{d}t} = \mathcal{P} + \mathcal{C}\,, \tag{12}$$

where $\mathcal{C} \equiv -\boldsymbol{\omega}\,\boldsymbol{\nabla}\cdot\mathbf{u}$ is the vorticity compression and $\mathrm{d}/\mathrm{d}t \equiv \partial/\partial t + \mathbf{u}\cdot\nabla$ is the convective derivative.

The circulation on the sinusoidal interface can be quantified by [38, 39]

$$\langle\omega\rangle(y, 0^+) \equiv \int_{-\infty}^{\infty} \omega(x, y, 0^+)\,\mathrm{d}x\,, \tag{13}$$

which can be compared to the predictions of the following analytical models.

1. In the Samtaney–Zabusky model [39] the circulation is

$$\langle\omega\rangle(y, 0^+) = \Gamma_1'\,k\,a_0\sin(k\,y)\,, \tag{14}$$

where

$$\Gamma_1' = \frac{c_{s1}}{Ma_s}\left[\frac{\gamma_2}{\gamma_2 - 1}\,\frac{1 - \phi(\frac{p_4}{p_2})}{\eta_0\,\gamma_1} - \frac{1 - \phi(\frac{p_5}{p_3})\,\phi(\frac{p_3}{p_1})}{\gamma_1 - 1}\right], \tag{15}$$

	Experimental initial conditions		Mix initial conditions	
Ma_i	1.292 ± 0.006		1.313	
$u_{shock,i}$ (cm/s)	38858		37311	
Δu (cm/s)	9260 ± 200		9770	
v_0 (cm/s)	1338.76		1336.8	
Ma_r	1.077		1.092	
$u_{shock,r}$ (cm/s)	34516		32203	
Ma_t	1.422		1.437	
$u_{shock,t}$ (cm/s)	19625		20265	
$t_{reshock}$ (ms)	6.00		5.65	
λ (cm)	5.9		5.9	
k (cm^{-1})	1.06495		1.06495	
η_c	–		0.738	
	Preshock	Postshock	Preshock	Postshock
a_0 (cm)	0.29	0.215	0.29	0.214
δ_T (cm)	0.5	–	0.5	0.369
At	0.605	0.635	0.605	0.604
ψ	1.17	1.131	1.182	1.133

Table 2: Comparison of the flow properties, including incident, reflected, and transmitted shock Mach numbers, Ma_i, Ma_r, and Ma_t, respectively, shock velocities $u_{\mathrm{shock},i}$, $u_{\mathrm{shock},r}$, and $u_{\mathrm{shock},t}$, respectively, interface velocity Δu, initial interface growth velocity v_0, and pre- and postshock initial amplitudes a_0^- and a_0^+, the pre- and postshock diffuse-interface width δ_T^- and δ_T^+, pre- and postshock Atwood numbers At^+, and At^-, and pre- and postshock growth reduction factor ψ^+ and ψ^-, when the initial conditions of Jacobs and Krivets are adopted in one-dimensional refraction theory. The results in the experiments of Jacobs and Krivets are compared with the results when a single value of the adiabatic exponent is used, corresponding to mix initial conditions.

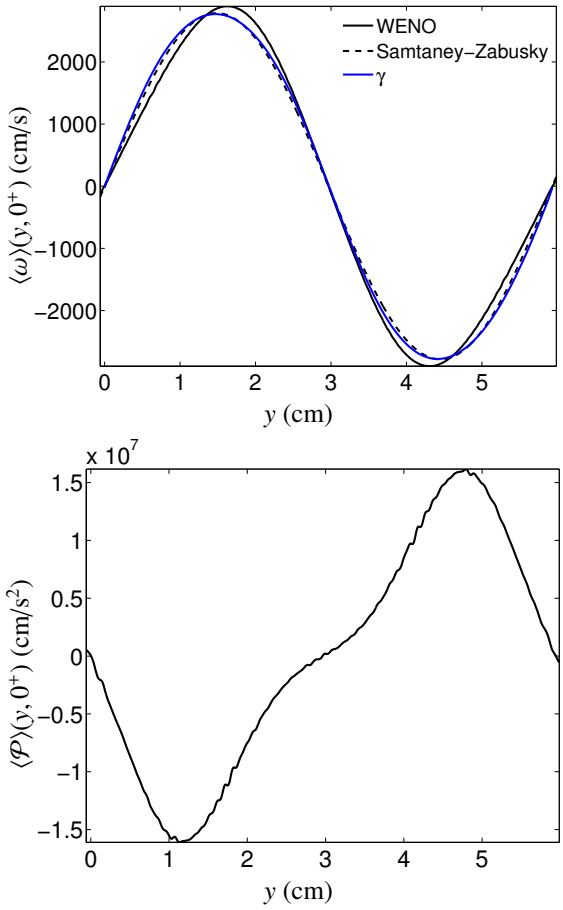

Figure 1: The initial deposition of circulation on the interface $\langle\omega\rangle(y,0^+)$ from the incident shock at time $t = 0^+$ from the WENO simulation (solid black line), together with the predictions of the Samtaney–Zabusky model (dashed line) and linear instability theory (solid blue line) (top). The average of the initial baroclinic vorticity production on the interface $\langle\mathcal{P}\rangle(y,0^+)$ is also shown (bottom).

$p_1 = p_2$ is the initial pressure ahead of the incident shock, p_3 is the pressure behind the incident shock, $p_4 = p_5$ is the pressure behind the reflected and transmitted shocks, η_0 is the initial density ratio, c_{s1} is the initial sound speed, and the ratio of sound speeds across the incident, reflected and transmitted shocks is given by $\sqrt{\phi(p_3/p_1)}$, $\sqrt{\phi(p_5/p_3)}$ and $\sqrt{\phi(p_4/p_2)}$, respectively, where $\phi(r) \equiv r(1+\mu r)/(\mu + r)$ and $\mu \equiv (\gamma+1)/(\gamma-1)$.

2. In the linear instability model [39], the vortex dipole and initial circulations are

$$\mu(e,0^+) = 2\,v_0 \cos\left[k\,x(e,0^+)\right] \cosh\left[k\,y(e,0^+)\right], \qquad (16)$$

$$\gamma(e,0^+) = \frac{\partial \mu(e,0^+)}{\partial e},$$

respectively, where v_0 [Eq. (3)] is the initial velocity and e is the parameter defining the two-dimensional interface.

The values of Γ_1', $\max(\gamma)$, and $\max\langle\omega\rangle$ are given in Table 3. Figure 1 shows the initial circulation deposited on the interface by the shock $\langle\omega\rangle(y,0^+)$ from the simulation, together with the prediction of the Samtaney–Zabusky model (14) and the linear instability model (16). The models give virtually identical predictions (0.6% difference), but underpredict the simulation results by $\approx$ 4%. The difference between the numerical and model predictions can be attributed to the fact that the circulation is computed at 0.06 ms. As a result, the initial circulation deposited on the interface has evolved, increasing in value in the proximity of the bubble and spikes.

The average of the baroclinic vorticity production term on the interface

$$\langle\mathcal{P}\rangle(y,0^+) \equiv \int_{-\infty}^{\infty} \mathcal{P}(x,y,0^+)\,\mathrm{d}x \qquad (17)$$

is also shown in Fig. 1. The shape of the curve is a skewed sinusoid. The baroclinic production mechanism can also be attributed to the evolution of this term on the interface, following the passage of the shock. The term could not have been computed at an earlier time, while the shock was crossing the interface.

3. Dynamics of the instability evolution

A two-dimensional simulation of a model of the Jacobs and Krivets [15] $Ma_i = 1.3$ air(acetone)/SF_6 shock tube experiment is performed using the ninth-order WENO method. The

	Max Circulation (cm/s)	Other Parameters
Samtaney–Zabusky	$\Gamma_1' \, a_0^+ = 2784.9$	$\Gamma_1' = 12952.9$ (1/s)
Linear instability	$\max(\gamma) = 2768.7$	
WENO	$\max[\langle\omega\rangle(y, 0^+)] = 2909.1$	$\max[\langle\mathcal{P}\rangle(y, 0^+)] = 1.6313 \times 10^7$ (cm/s^2)

Table 3: Predictions of the Samtaney–Zabusky and linear instability models and comparison to WENO results. Also shown is $\max[\langle\mathcal{P}\rangle(y, 0^+)]$, which quantifies the initial circulation deposition on the interface.

grid resolution and other numerical parameters are given in Table 6. Simulations for a similar two-dimensional, single-mode Richtmyer–Meshkov instability with reshock using the same code with different grid resolutions and comparison of results are discussed in detail elsewhere [22]. The density fields from the simulation are compared to the experimental planar laser-induced fluorescence (PLIF) images in Sec. 3.1. In addition, the mass fraction contour from these simulations is compared. The vorticity and baroclinic vorticity production $\mathcal{P}$ fields are also discussed in Sec. 3.2. The vorticity can be interpolated onto the mass fraction contour to give the vortex sheet strength on the interface.

3.1. Comparison of density fields to experimental PLIF images

Figure 2 shows a comparison of the density fields from the simulation with the PLIF images from the Jacobs–Krivets experiment. At 1.16 ms, the simulation gives a similar characterization of the bubble and spike initial growth as in the experiment. At 3.06 and 5.26 ms, the roll-up in the simulation shows additional small-scale structure along the interface and within the vortex cores (which may be attributable to the absence of molecular dissipation and diffusion). The overall morphology of the bubbles and spikes (including the widths of the stem and troughs) are in very good agreement between the simulation and experiment. The WENO method shows a fully-developed roll-up with fragmentation, which is clearly visible in the density field.

3.2. Visualization of the vorticity and baroclinic vorticity production fields

Figure 3 shows the vorticity $\omega(x, y)$ and baroclinic vorticity production $\mathcal{P}(x, y)$ fields from the simulation. At 0.06 ms, the vorticity field shows one layer of positive and negative vorticity deposited by the shock. The vorticity indicates that the linear instability model best characterizes the diffuse interface of the Jacobs and Krivets experiment and the diffuse interface of the simulation. The initial baroclinic vorticity production shows the reduction of vorticity near the bubble tip and the increase of vorticity near the spike tip. At 1.16 ms, there is a stronger concentration of vorticity corresponding to the roll-up region. The baroclinic vorticity production also shows that more generation occurs near the spike tip. At 3.06 and 5.26 ms the simulation shows fragmentation surrounding the main rotating core, produced by the secondary vortex accelerated vorticity deposition, which is related to baroclinic vorticity production. Most of the baroclinic vorticity production is concentrated near the cores and along the interface.

Additional thin structure in the vorticity forms above the main interface. These are visible as faint lines at times 1.16 and 3.06 ms and then develop into additional structures that are visible at 5.26 ms. These structures are due to the pressure fluctuations originating from the reflected rarefaction wave, which together with the accompanying density fluctuations, induces a nonzero vorticity compression C in Eq. (12). The vorticity field is also advected away from the interface.

4. Comparison of the perturbation, bubble, and spike amplitudes to experimental data and model predictions

Here, the amplitude and bubble and spike velocity are compared to the predictions of several nonlinear growth models. Nonlinear Padé models for the amplitude growth are discussed in Sec. 4.1, and models for the bubble and spike velocities are presented in Sec. 4.2. A comparison of the amplitudes from the numerical simulation to experimental results and to the predictions of the models is discussed in Sec. 4.3.

4.1. Nonlinear Padé models

Models based on asymptotic expansion of the linear perturbation equations are briefly summarized here. These models generate asymptotic series with limited radii of convergence: the convergence is improved using Padé approximants.

Zhang and Sohn [40] developed a model for the growth of a two-dimensional Richtmyer–Meshkov unstable interface from early to late times for a reflected shock (light-to-heavy transition). The dynamics of the interface are modeled using the linear, compressible flow equations for early times and the nonlinear, incompressible flow equations for later times. This formulation gives an independent series for the spike and bubble amplitudes in terms of the Richtmyer velocity v_0 [Eq. (3)]. As the range of validity of this finite Taylor series approximation is limited, Padé approximations are used to extend the approximation into the nonlinear regime to give the amplitude

$$a(t) = a_0 + \frac{2}{k\sqrt{4\max\left[0, (k\,a_0)^2 - At^2 + \frac{1}{2}\right] - (k\,a_0)^2}} \times \tan^{-1}\left[\frac{k\,a_0 + 2\max\left[0, (k\,a_0)^2 - At^2 + \frac{1}{2}\right] k\,v_0\,t}{\sqrt{4\max\left[0, (k\,a_0)^2 - At^2 + \frac{1}{2}\right] - (k\,a_0)^2}}\right]. \quad (18)$$

The choice of the Padé approximants matches the experimental late-time growth. However, the Zhang–Sohn model does not predict the generally accepted $1/t$ velocity decay at late times.

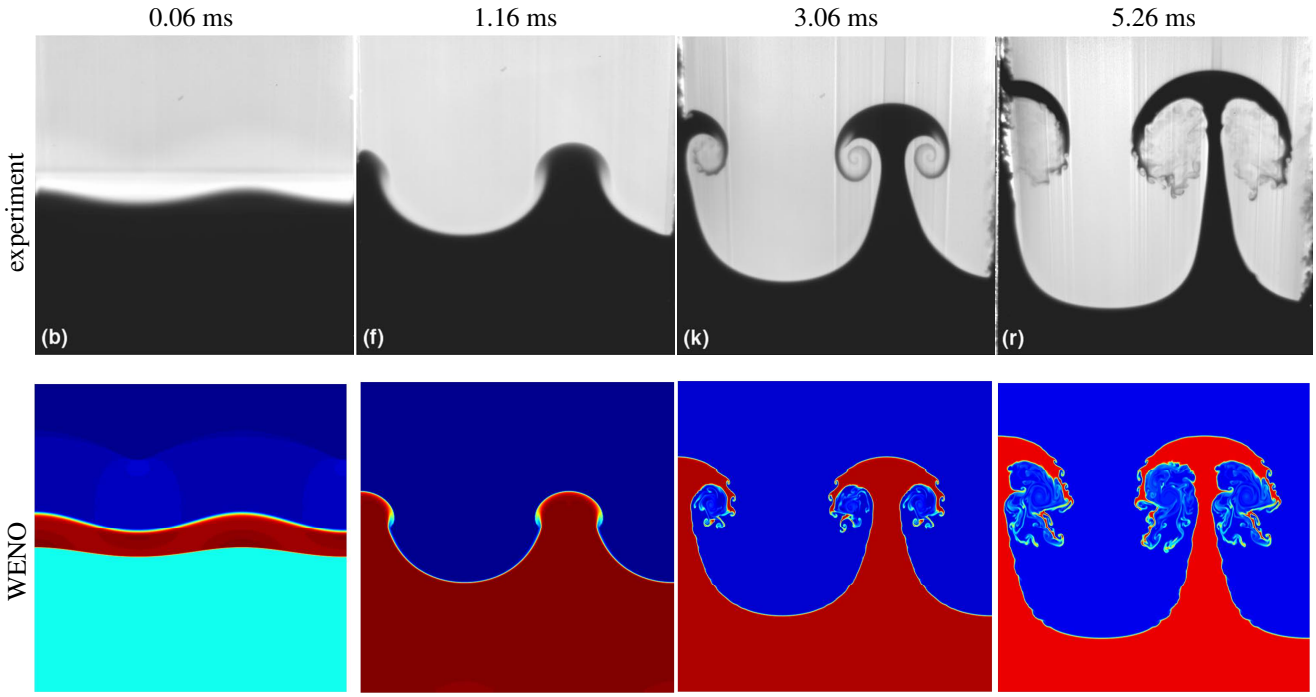

Figure 2: Comparison of the corrected PLIF images from the Jacobs–Krivets experiment with the density fields $\rho(x, y)$ from the WENO simulation at a resolution of 512 points per wavelength at 0.06, 1.16, 3.06, and 5.26 ms. The experimental images are reproduced from Fig. 5 of Jacobs and Krivets [15] (with the permission of AIP Publishing).

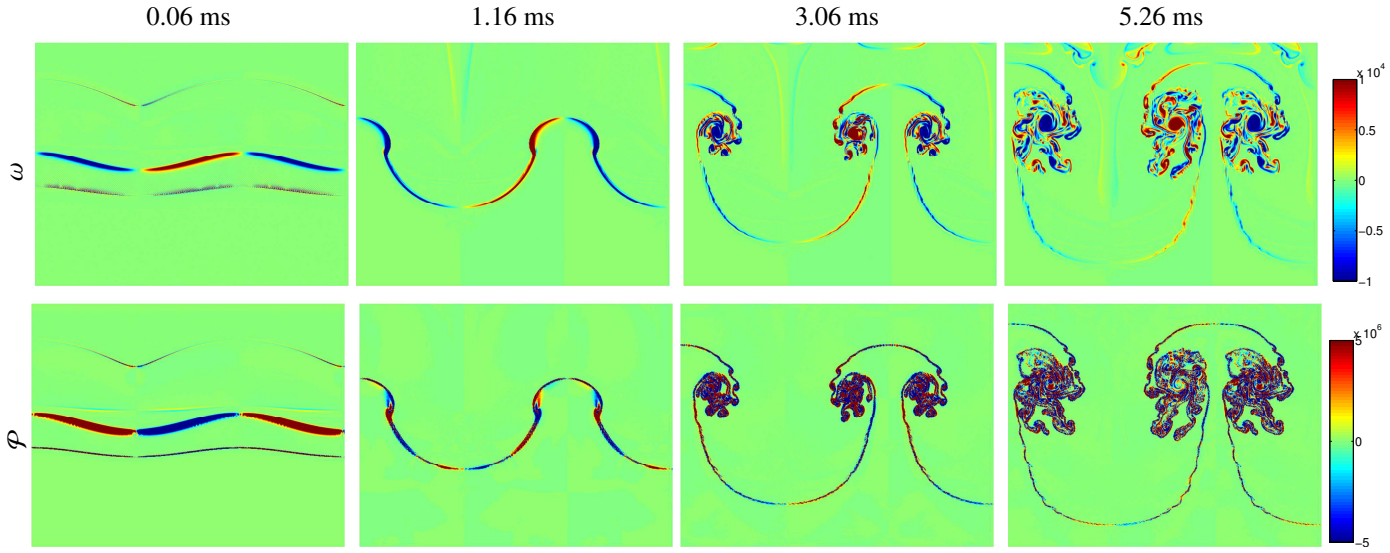

Figure 3: The vorticity fields $\omega(x, y)$ (top row) and the baroclinic vorticity production fields $\mathcal{P}(x, y)$ (bottom row) from the WENO simulation at 0.06 , 1.16, 3.06, and 5.26 ms.

The empirical Sadot et al. [31] model is based on fits to Richtmyer–Meshkov instability experimental data and on asymptotic growth laws. This model was tested against experimental data and appears to be valid over Mach numbers 1.3–3.5 in air and SF_6. The model provides a single formula that describes the initial linear growth and the later nonlinear growth of the bubble and spike,

$$v_{b,s}(t) = \frac{\mathrm{d}a_{b,s}}{\mathrm{d}t} = \frac{(1 + k\,v_0\,t)\,v_0}{1 + (1 \pm At)\,k\,v_0\,t + \frac{1 \pm At}{1+At}\,\frac{(k\,v_0\,t)^2}{2\pi\,C}}\,, \qquad (19)$$

where $C = 1/(3\pi)$ for $At \geq 0.5$ (with + and − corresponding to the bubble and spike, respectively). In the limit $At \to 0$, $C = 1/(2\pi)$. Integrating Eq. (19) gives the bubble and spike amplitudes

$$\begin{aligned} a_{b,s}(t) \;=\; & a_{b,s}(0) + \frac{2 - 2\pi\,C\,(1 + At)}{k\,\sqrt{\frac{2}{\pi\,C}\,\frac{1 \pm At}{1+At} - (1 \pm At)^2}} \\ & \times \tan^{-1}\left[\frac{1 \pm At + \frac{1 \pm At}{1+At}\,\frac{k\,v_0\,t}{\pi\,C}}{\sqrt{\frac{2}{\pi\,C}\,\frac{1 \pm At}{1+At} - (1 \pm At)^2}}\right] \\ & + \frac{\pi\,C}{k}\,\frac{1 + At}{1 \pm At} \\ & \times \ln\left[1 + (1 \pm At)\,k\,v_0\,t + \frac{1 \pm At}{1 + At}\,\frac{(k\,v_0\,t)^2}{2\pi\,C}\right]. \end{aligned} \qquad (20)$$

This model is consistent with the $1/t$ asymptotic decay of the velocity at late times.

Matsuoka, Nishihara, and Fukuda [41] proposed a new formulation of the kinematic boundary conditions in the perturbation expansion of the Zhang–Sohn potential flow model to account for stretching at the interface. This provides different expansions for the bubble and spike velocity

$$\frac{\partial a_{b,s}}{\partial \tau} = \frac{f_\pm^3}{\left[f_\pm\left(At^2 - \frac{1}{2}\right) + g_\pm^2\right]\tau^2 - f_\pm\,g_\pm\,\tau + f_\pm^2}\,, \qquad (21)$$

where $f_\pm \equiv \mp\left(2At^2 - 3/2\right)(ka_0)^2 + ka_0 At/2 \mp 1$, $g_\pm \equiv \mp 2At^2 ka_0 + At \pm ka_0$, and $\tau = kv_0 t$ is the rescaled time (with + and − corresponding to the bubble and spike, respectively).

Mikaelian [42] obtained an analytic expression for the transition of the bubble amplitude from the linear to nonlinear regime by combining the Richtmyer initial velocity v_0 [Eq. (3)] with the Goncharov late-time bubble growth for arbitrary Atwood numbers [see Eq. (23) below]. Mikaelian combined the initial and asymptotic bubble velocities with a transition between these velocities at time t^* where $a_b(t^*) = 1/(3k)$. This results in a bubble amplitude

$$a_b(t) = \frac{1}{3\,k}\left\{1 + \frac{3 + At}{1 + At}\,\ln\left[1 + \frac{3\,k\,v_0\,(1 + At)}{3 + At}(t - t^*)\right]\right\} \qquad (22)$$

for times $t > t^*$, so that v_b agrees with the Goncharov model (23) at large times.

4.2. Bubble and spike velocity models

Bubble and spike velocity models are derived from potential flow models and are valid through the late-time, nonlinear regime. Layzer [43] developed the first potential flow model to describe Rayleigh–Taylor instability, which was subsequently extended to Richtmyer–Meshkov instability. These models predict that the bubble and spike velocities approach zero asymptotically.

Goncharov [44] extended the two-dimensional Layzer model to the $At \neq 1$ case using a parabolic expansion near the bubble and spike tips and an ansatz for the initial velocity potential. This ansatz requires the solution of five ordinary differential equations, giving the asymptotic bubble velocity

$$v_b(t) = \frac{3 + At}{3\,(1 + At)\,k\,t}\,. \qquad (23)$$

Sohn [45] also extended the Layzer model to fluids with arbitrary density ratios. The approach differs from that of Goncharov in the use of a simpler form for the initial velocity potentials, leading to a simplified system of three ordinary differential equations. The Sohn–Layzer asymptotic bubble velocity is

$$v_b(t) = \frac{2}{(2 + At)\,k\,t}\,. \qquad (24)$$

The predictions of the Sohn–Layzer and Goncharov models are very similar.

Sohn [46] also extended the Zufiria model [47, 48] to arbitrary Atwood numbers. In the Zufiria model, the velocity potential is obtained by approximating the bubble as a point source. The Sohn–Zufiria bubble velocity is

$$v_b(t) = \left[\frac{3 + At}{3\,(1 + At)} - \frac{1}{q} + \frac{2\,At}{3\,(1 + At)\,q^2}\right]\frac{1}{k\,t}\,, \qquad (25)$$

where $q = q(At)$ is the root of the cubic polynomial $(3 - At)\,q^3 - (21 + 9At)\,q^2 + (3 + 15At)\,q - 4At = 0$. Comparing the Sohn–Zufiria model (25) with the Goncharov model (23) shows that the former contains two additional terms, resulting in a smaller asymptotic velocity.

Zhang and Guo [49] recently proposed a universal model for the spike and bubble velocity

$$v_{b,s}(t) = \frac{v_0}{1 + \alpha\,k\,v_0\,t}\,, \qquad (26)$$

where v_0 is the Richtmyer velocity, Eq. (3), and

$$\alpha = \frac{3}{4}\,\frac{(1 + At)(3 + At)}{3 + At + \sqrt{2 + 2\,At}}\,\frac{4\,(3 + At) + (9 + At)\,\sqrt{2 + 2\,At}}{(3 + At)^2 + 2\,(3 - At)\,\sqrt{2 + 2\,At}}\,. \qquad (27)$$

Equation (26) is universal because α is computed for the bubble using $At < 0$ and for the spike using $At > 0$. Integrating Eq. (26) gives the bubble and spike amplitudes

$$a_{b,s}(t) = \frac{\ln\,(1 + \alpha\,k\,v_0\,t)}{\alpha\,k}\,. \qquad (28)$$

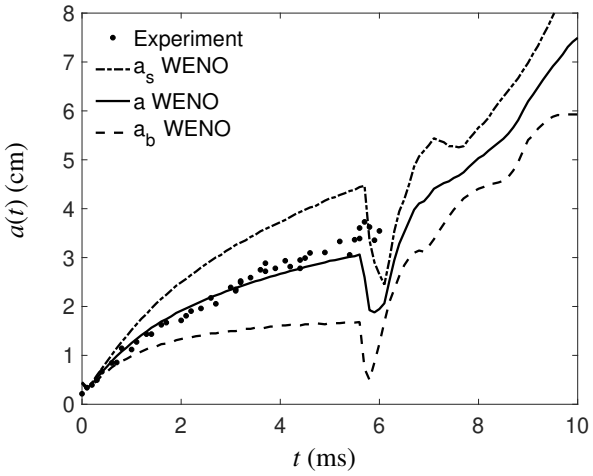

Figure 4: Comparison of the perturbation amplitude $a(t)$ from the WENO simulation with the experimental data points. Also shown are the bubble and spike amplitudes $a_b(t)$ and $a_s(t)$, respectively.

4.3. Comparison of simulation amplitudes to experimental data and to predictions of nonlinear growth models

Presented here is a comparison of the perturbation, bubble, and spike amplitudes from the simulation using 512 points per initial perturbation wavelength with the experimental data points of Jacobs and Krivets and the predictions of the previously discussed amplitude growth models. The perturbation amplitude is the difference between the bubble and spike locations. The bubble and spike locations are calculated from the mass fraction $m(x, y)$ (see Ref. [22] for details). To determine the bubble and spike amplitudes, a numerical simulation without an initial perturbation (but otherwise identical) was performed to obtain the interface location. The difference between the bubble and interface location gives the bubble amplitude, and the difference between the interface and spike location gives the spike amplitude.

Figure 4 shows a comparison of the perturbation amplitude $a(t)$ from the simulation with the experimental data points. There is good agreement between the simulation results and the experimental data points. It is apparent that there is a strong asymmetry between the bubble and spike amplitudes (nearly a factor of two difference).

When comparing the simulation data to the predictions of the models, the amplitude growth rate is adjusted to account for the diffuse interface by including the growth reduction factor (11). Shown in Fig. 5 is a comparison of the perturbation amplitude from the WENO simulation with the experimental data points and the predictions of the nonlinear Zhang–Sohn series model (18), the Matsuoka et al. series model (21), the nonlinear Sadot et al. model (20), and the Zhang–Guo model (28). The Sadot et al. model overpredicts the perturbation amplitude, while the Zhang–Sohn and Matsuoka et al. models underpredict the amplitude. The Sadot et al. model gives the best overall agreement with the simulation data.

Figure 6 shows the velocity, bubble velocity, and spike velocity from the simulation together with the corresponding predic-

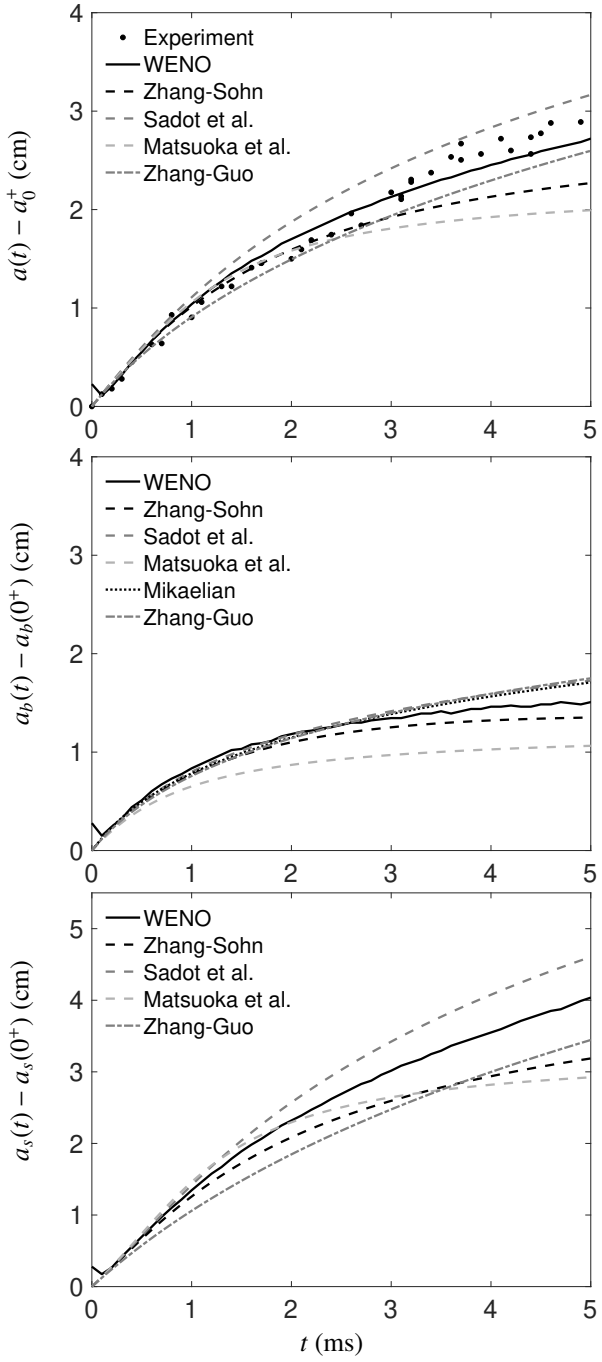

Figure 5: The perturbation amplitudes $a(t) - a_0^+$ (top), $a_b(t) - a_b(0^+)$ (middle), and $a_s(t) - a_s(0^+)$ (bottom) versus time t from the WENO simulation and the experimental data points, together with the predictions of the nonlinear growth models.

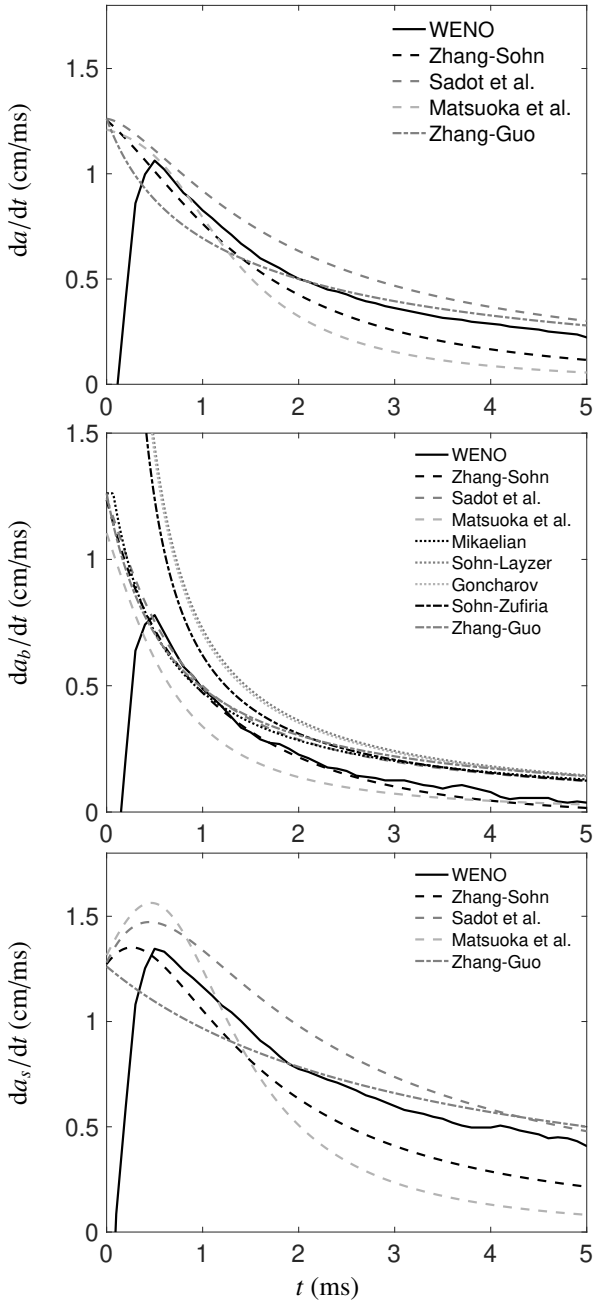

Figure 6: Comparison of the WENO velocities $\mathrm{d}a(t)/\mathrm{d}t$ (top), $\mathrm{d}a_b(t)/\mathrm{d}t$ (middle), and $\mathrm{d}a_s(t)/\mathrm{d}t$ (bottom) with the predictions of the Zhang–Sohn, Sadot et al., Matsuoka et al., Mikaelian, Sohn–Layzer, Goncharov, Sohn–Zufiria, and Zhang–Guo models.

	Δ_{exp}	Δ_{sim}
Experiment	–	6.35
Zhang–Sohn Padé (all)	13.0	9.9
Zhang–Sohn Padé (bubble)	–	5.2
Zhang–Sohn Padé (spike)	–	12.2
Matsuoka et al. Padé (all)	19.4	14.9
Matsuoka et al. Padé (bubble)	–	22.5
Matsuoka et al. Padé (spike)	–	12.7
Sadot et al. (all)	11.7	9.6
Sadot et al. (bubble)	–	6.0
Sadot et al. (spike)	–	11.5
Mikaelian (bubble)	–	5.2
Zhang–Guo (all)	10.0	10.4
Zhang–Guo (bubble)	–	6.8
Zhang–Guo (spike)	–	19.9

Table 4: Average fractional deviations Δ_{exp} between the experimental amplitude $a_{\mathrm{exp}}(t)$ and the amplitude from the WENO simulation a_{sim} and the predictions of the nonlinear models $a_{\mathrm{mod}}(t)$, respectively. Also shown is the average fractional deviation Δ_{sim} between the simulation amplitude $a_{\mathrm{sim}}(t)$ and the amplitude from the nonlinear models $a_{\mathrm{mod}}(t)$.

tions from the models. Also shown are the asymptotic bubble velocities from the the Sadot et al. model (20), the Matsuoka et al. model (21), and the Zhang–Guo model (28). The simulation velocities are best described by the Sadot et al. and Zhang–Sohn models.

To quantitatively compare the agreement between the simulation and model perturbation amplitude and the n experimental data points shown in Fig. 5, the average fractional deviations [11, 15]

$$\Delta_{\mathrm{exp}} = \frac{1}{n}\sum_{i=1}^{n}\frac{\left|a_{\mathrm{mod}}(t_i) - a_{\mathrm{exp}}(t_i)\right|}{a_{\mathrm{exp}}(t_i)}\,, \tag{29}$$

$$\Delta_{\mathrm{sim}} = \frac{1}{n}\sum_{i=1}^{n}\frac{\left|a_{\mathrm{mod}}(t_i) - a_{\mathrm{sim}}(t_i)\right|}{a_{\mathrm{sim}}(t_i)}\,, \tag{30}$$

are shown in Table 4, with smaller values of Δ_{exp} and Δ_{sim} indicating better agreement. The simulation data agrees very well with the experimental data points on average. The average fractional deviations between the WENO simulation and the nonlinear model predictions indicate that the overall perturbation and spike amplitudes are best captured by the Sadot et al. model, and the bubble amplitude is best captured by the Zhang–Sohn model. Note that Δ_{sim} is systematically larger for the spikes compared to the bubbles.

The time-evolution of the circulation and resolution-dependent numerical Reynolds number [22]

$$Re_{\Delta x}(t) = \left[\frac{a(t)}{\Delta x}\right]^{4/3}\,, \tag{31}$$

where $a(t) = a_b(t) + a_s(t)$, are shown in Fig. 7. During the early-time evolution, the circulation decreases slightly and then steadily grows linearly with time; the rate of growth sharply decreases at the time of reshock. The numerical Reynolds number grows relatively slowly as a power-law before reshock, decreases as the mixing layer is compressed during reshock, and

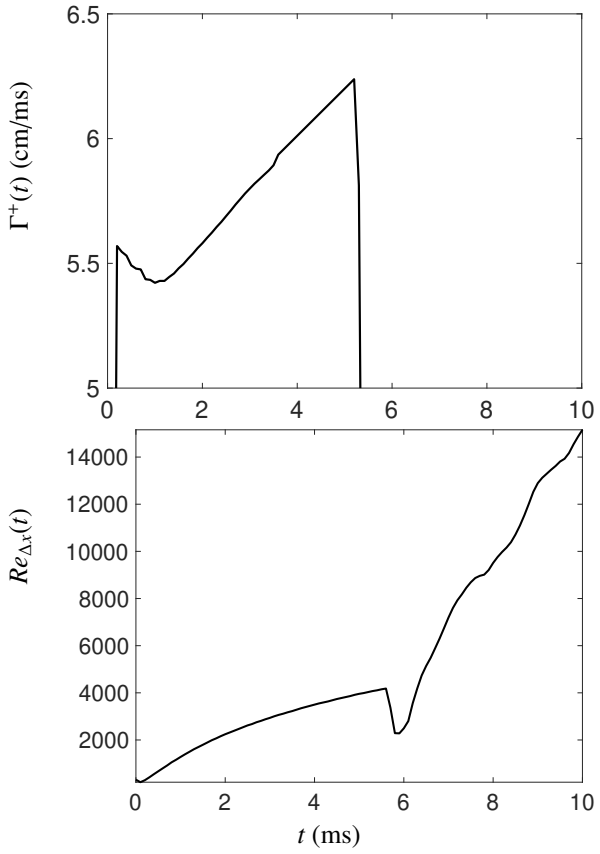

Figure 7: Time-evolution of the circulation $\Gamma^+(t)$ and numerical Reynolds number $Re_{\Delta x}(t)$ from the WENO simulation.

then grows much more rapidly following reshock, attaining a value of $\approx 1.5 \times 10^4$ at the latest time.

5. Analysis of two-dimensional reshock

Figure 8 shows the x-t diagram from the WENO simulation. The locations of the bubble $\ell_b(t)$ and of the spike $\ell_s(t)$ are shown using the dash-dot and the dashed lines, respectively. The interface location is also shown using a solid line. The horizontal distance between the spike and bubble is the perturbation width $h(t)$, and half of this distance is the perturbation amplitude $a(t)$. Reshock occurs at $\approx$ 5.65 ms, when the shock wave refracts at the evolving interface, generating a transmitted shock in the air(acetone), and a reflected rarefaction wave returns into the SF_6.

The transmitted shock following reshock moves faster than the incident shock, as indicated by the change in the slope, corresponding to a slow–fast refraction [50]. Following reshock, the interface is compressed (as indicated by the kink in the bubble and spike locations) and moves away from the end wall of the test section. The reflected rarefaction wave returning back into the SF_6 is not shown in the x-t diagram. This rarefaction reflects from the end wall of the test section and interacts with the interface at $\approx$ 8.5 ms, inducing an expansion of the interface (as shown from the position of the bubble and spikes) and

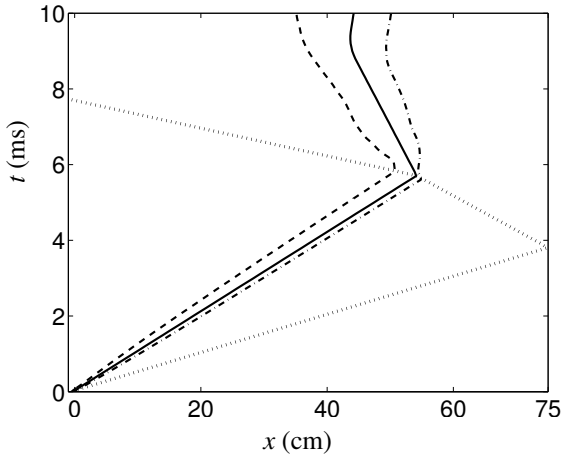

Figure 8: The x-t diagram showing the position of the interface $\ell_{\text{int}}(t)$ (solid line), shock (dotted line), and bubble and spike locations $\ell_b(t)$ and $\ell_s(t)$ (dash-dot and dashed lines, respectively). The horizontal distance between the spike and the bubble location is the perturbation width $h(t)$.

causing the interface to move towards the end wall. The interaction with the reflected rarefaction causes a compression wave to return into the SF_6, and a series of wave interactions follows until the interface eventually comes to rest in the shock tube test section.

5.1. Dynamics of the reshock process

Figure 9 shows the time-evolution of the density and simulated density schlieren fields during reshock at time intervals of 0.1 ms (and later 0.2 ms) from 5.6 to 7 ms. Simulated density schlieren images are used to visualize the detailed wave structure present during reshock. The density schlieren shown is [51]

$$\Phi(x,y,t) = \exp\left[-\alpha(m)\,\frac{|\nabla\rho|}{\max|\nabla\rho|}\right],\ \alpha(m) = \begin{cases} 20 & \text{if } m > m^*, \\ 100 & \text{if } m < m^*, \end{cases} \tag{32}$$

where m is the mass fraction of SF_6 and $m^* = 0.25$.

Figure 9 shows the arrival of the reflected shock at 5.6 ms, the reflected shock refracting at the interface at 5.7 ms and at 5.8 ms, and the inception of the inversion process at 5.9 ms, when bubbles transform into spikes and vice versa. As reshock here is a refraction from a heavier fluid (SF_6) into a lighter fluid [air(acetone)], a transmitted shock enters the air(acetone) and a reflected rarefaction wave returns back into the SF_6. The transmitted shock is highly curved following the interaction with the bubble at 5.7 ms, and also generates a complex system of waves as it passes through the roll-ups at 5.8 and 5.9 ms. The inversion occurs due to the deposition of vorticity of opposite sign on the interface that drives the formation of rolls-up in the opposite direction.

The simulated density schlieren not only provides a detailed visualization of the system of reflected and transmitted waves generated during reshock, but also clearly shows the fine-scale mixing within the roll-ups and more generally within the mixing layer. In particular, prior to reshock, the cores of the roll-up

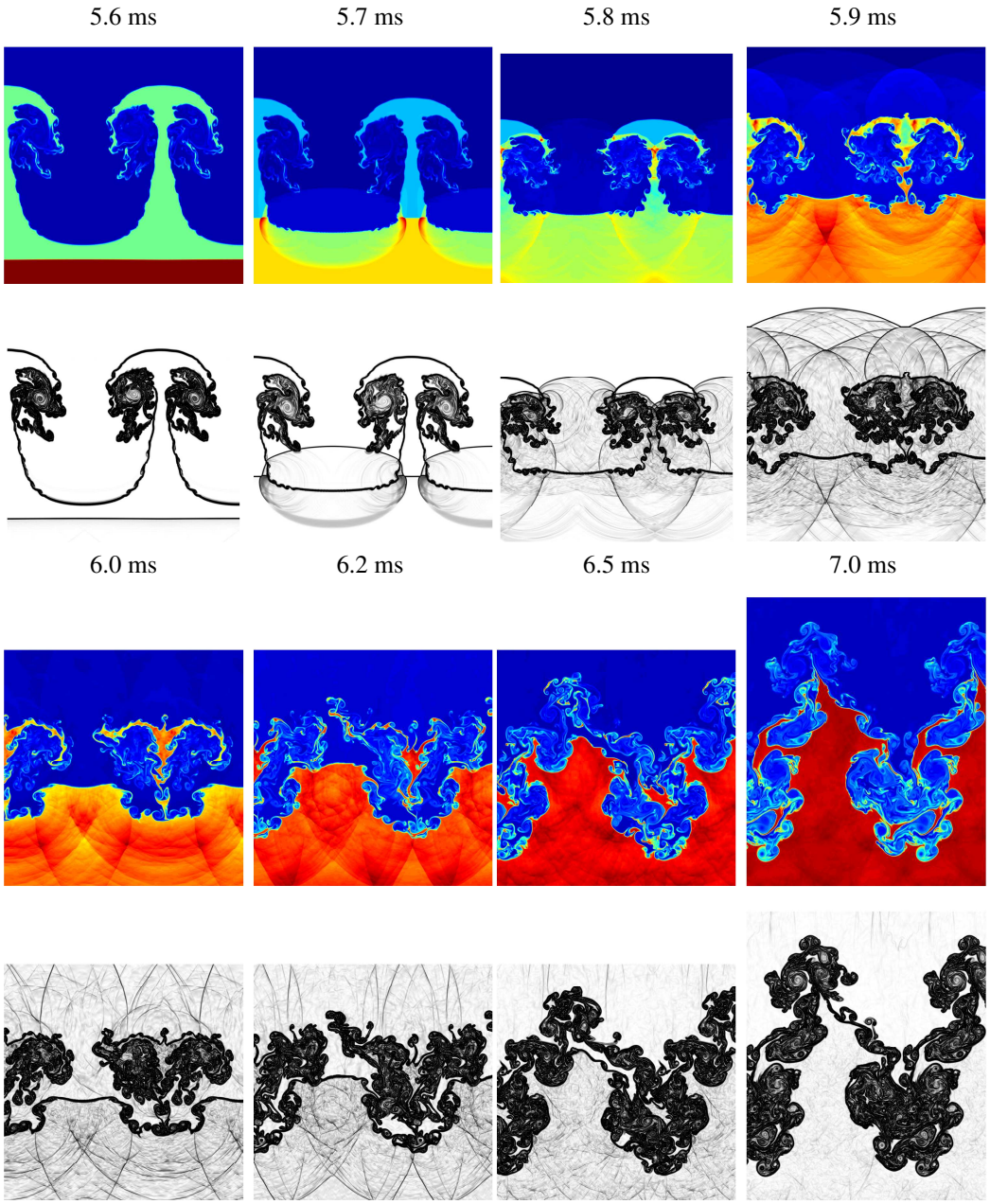

Figure 9: Time-evolution of the density and simulated density schlieren fields from the WENO simulation illustrating the reshock process at 5.6, 5.7, 5.8, 5.9, 6.0, 6.2, 6.5, and 7.0 ms.

contain well-mixed complex regions. During reshock, these regions are compressed by the passage of the shock. At late times, large spikes of SF_6 develop. Near the large spike, a finely-mixed complex layer is observed, which are the remnants of the spike prior to reshock. The creation of small disordered structures breaks symmetry [12], leading to the formation of complex structures with a wide range of scales at late times. Note that the 'mixing' described here is induced by numerical processes, but is largely consistent with the mixing observed experimentally.

Figure 10 shows the time-evolution of the vorticity $\omega(x, y)$ and baroclinic vorticity production field $\mathcal{P}(x, y)$ at the same times as in Fig. 9. Immediately prior to reshock (5.6 ms), strong rotating cores develop, together with the vortex bilayers that contribute to the formation of the irregular structures within the roll-ups. At 5.7 ms, vorticity of opposite sign is deposited by the shock on the interface and drives the inversion process at 5.8 and 5.9 ms. The vorticity deposited by the shock is eight times more intense than the vorticity present inside the roll-ups. As a result, at 5.7 ms the vorticity inside the roll-ups appears much smaller. By contrast, the baroclinic vorticity production experiences more than a ten-fold increase at reshock, and the baroclinic production inside the roll-ups is almost not apparent at 5.7 ms. Following passage of the transmitted shock, the baroclinic vorticity production forms strong positive and negative cores around the roll-up, contributing to the further fragmentation and increased mixing within the layer, as shown by the simulated density schlieren.

The baroclinic vorticity production also contributes to the formation of strong vortex bilayers. As a result, the layers of negative (or positive) vorticity present immediately following the passage of the shock at 5.9 ms on the surface of the spike are replaced by a disordered set of alternating layers of positive and negative vorticity at 6.0 ms. After 6.0 ms, the inversion process forms a strong spike that penetrates into the mixing layer. A region of finely-mixed material forms where the pre-reshock spike was previously located. The presence of the numerous vortex bilayers in the region previously occupied by the spike may facilitate the penetration of the spike, which instead has a strong region of positive and negative vorticity and behaves as a "vortex projectile" [4]. This may also elucidate why spikes penetrate deeply into the mixing layer at 6.2 and 6.5 ms. At late times, larger-scale structures form due to the inverse energy cascade [12].

Finally, Fig. 11 shows the density, vorticity, and baroclinic vorticity production fields at late times following reshock. The simulation produces highly complex structures at late times. A dominant spike is present, and finely-mixed fluid is present in between the structures. The vorticity field shows the formation of localized strong cores of positive and negative vorticity. The baroclinic vorticity production shows fragmentation and activity that occurs at the boundaries of the large-scale structure and in between the separation region.

5.2. Comparison of the mixing layer amplitude to the predictions of reshock models

Here, the mixing layer amplitude from the WENO simulation is compared to the predictions of several reshock models. A similar comparison was performed previously [12] using a two-dimensional WENO simulation of a model of the Collins and Jacobs experiment [30].

A linear power-law model for the mixing layer amplitude following reshock was developed by Mikaelian [52]

$$\frac{\mathrm{d}a}{\mathrm{d}t} = 0.14\,\Delta u_1\,At_1^+\,, \tag{33}$$

where At_1^+ is the post-reshock Atwood number, based on the experimental results of Read [53] and Youngs [54] for the width of a Rayleigh–Taylor mixing layer. The numerical prefactor is obtained from the assumed value of the Rayleigh–Taylor mixing growth parameter $\alpha = 0.14$ in the self-similar mixing layer width expression $h(t) = \alpha Atgt^2$ (where g is the constant acceleration).

Brouillette and Sturtevant [55] performed shock tube experiments to assess the effects of a thick, diffuse interface on the growth of Richtmyer–Meshkov instability. The expression

$$\frac{\mathrm{d}a}{\mathrm{d}t} = k\left(a_0^+\,\Delta u\,At^+ + a_1^+\,\Delta u_1\,At_1^+\right) \tag{34}$$

was obtained by empirically generalizing the Richtmyer model, where the subscript 1 indicates values following reshock.

Charakhch'yan [56] assumed that reshock is much weaker than the initial incident shock and occurs during the nonlinear phase, to obtain

$$\frac{\mathrm{d}a}{\mathrm{d}t} = u_1^- - 1.25\,\Delta u_1\,At^+\,, \tag{35}$$

where u_1^- is the pre-reshock velocity. The reshock growth does not depend on the initial amplitude and on the change in Atwood number at reshock (i.e., it depends on At^+ rather than on At_1^+).

Lombardini et al. [57] developed a semi-analytical, impulsive model based on a diffuse-interface approach [58]. The model is (written here for the amplitude)

$$\frac{\mathrm{d}a}{\mathrm{d}t} = \frac{C'}{2}\,(At_1^+)^2\,g(At_1^+)\,\Delta u_1\,, \tag{36}$$

$$g(At_1^+) = \frac{1}{\left(At_1^+\right)^2}\left[1 - \frac{1-\left(At_1^+\right)^2}{2\,At_1^+}\log\left(\frac{1+At_1^+}{1-At_1^+}\right)\right]$$

with the coefficient $C' \approx 0.6$ determined using comparisons to data from their large-eddy simulations.

Figure 12 shows the mixing layer amplitude and the predictions of the Mikaelian, Brouillette–Sturtevant, Charakhch'yan, and Lombardini et al. reshock models. All of these models predict linear growth in time. The Brouillette–Sturtevant model predicts the largest velocity, followed by the Mikaelian, Lombardini et al., and the Charakhch'yan models. The models are intended to apply immediately after reshock ($\approx$ 5.77 ms) until

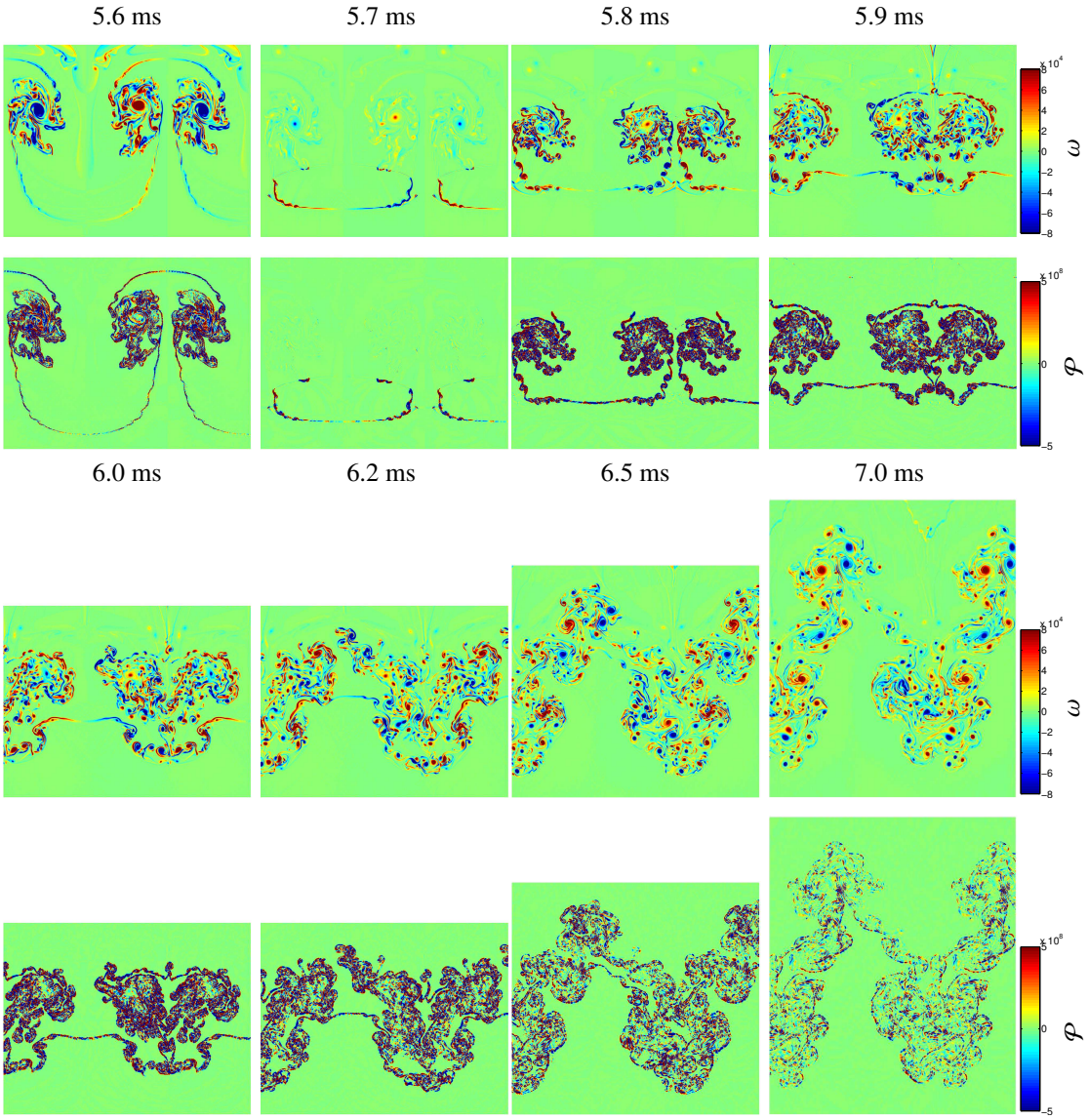

Figure 10: Time-evolution of the vorticity $\omega(x, y)$ and baroclinic vorticity production $\mathcal{P}(x, y)$ fields from the WENO simulation during reshock at 5.6, 5.7, 5.8, 5.9, 6.0, 6.2, 6.5, and 7.0 ms.

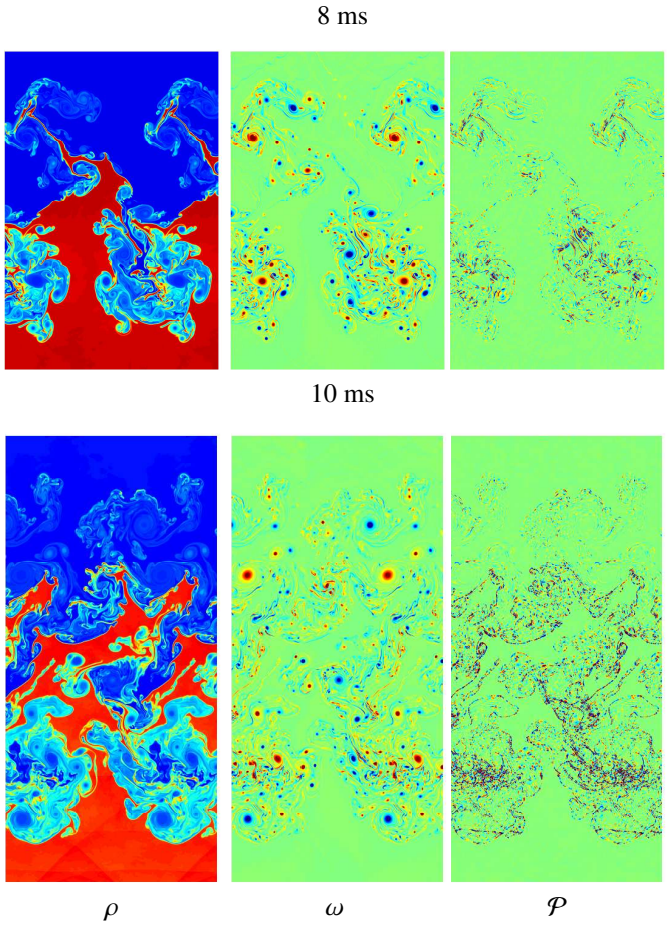

Figure 11: Time-evolution of the density $\rho(x, y)$, vorticity $\omega(x, y)$, and baroclinic vorticity production $\mathcal{P}(x, y)$ fields from the WENO simulation at 8 and 10 ms.

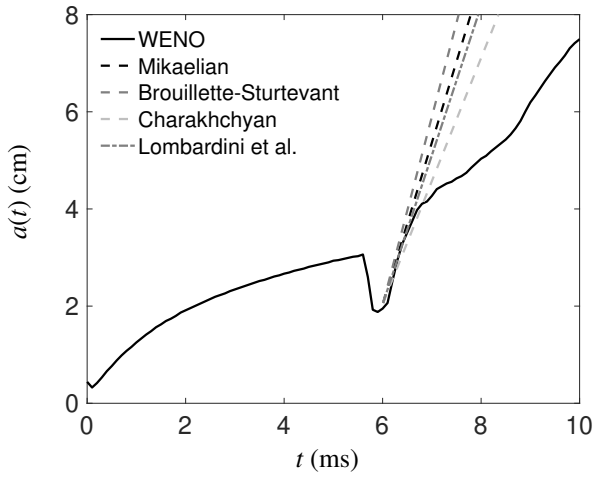

Figure 12: The mixing layer amplitude $a(t)$ versus time t from the WENO simulation together with the predictions of the linear reshock models.

2D Simulation	$\frac{da}{dt}$	$k\,\frac{da}{d\tau}$
Richtmyer	1337	1
Mikaelian	3334	2.50
Brouillette–Sturtevant	3871	2.89
Charakhch'yan	2534	1.89
Lombardini et al.	3071	2.30

Table 5: The velocity da/dt (in units of cm/ms) and the normalized velocity $kda/d\tau$ from the Richtmyer model before reshock for mix initial conditions. Also shown is the velocity and the normalized velocities from the Mikaelian, Brouillette–Sturtevant, Charakhch'yan, and Lombardini et al. reshock models.

the arrival of the reflected rarefaction wave at ≈ 7.0 ms. The model predictions are in good agreement with the simulation data. The mixing layer amplitude velocities da/dt and the normalized velocities $kda/d\tau$ are given in Table 5.

6. Three-dimensional single-mode Richtmyer–Meshkov instability

Presented here are three-dimensional WENO simulations of single-mode Richtmyer–Meshkov instability using two values of the initial perturbation amplitude and analysis of the results.

6.1. Initial and boundary conditions

The initial and boundary conditions in three dimensions are similar to those in two dimensions (see Table 6) with the values for the periodic z direction the same as those for the periodic y direction: $L_z = L_y$, $\Delta z = \Delta y$, and $N_z = N_y$. The initial perturbation

$$\eta(y, z) = a_0^- \sin\left(k_y\, y\right) \sin\left(k_z\, z\right) \tag{37}$$

is the standard initial condition for single-mode Richtmyer–Meshkov instability in three dimensions. For example, it was previously used in the quantitative study of three-dimensional Richtmyer–Meshkov instability [59] and in a comparison between two- and three-dimensional simulations [60].

As $k_y = k_x = k_{2D}$, the effective wavenumber for the three-dimensional perturbation is

$$k_{3D} = \sqrt{k_x^2 + k_y^2} = \sqrt{2}\, k_{2D}\,. \tag{38}$$

Thus, two values for the initial preshock amplitude are considered:

1. $a_0^- = 0.205$ cm, such that the preshock amplitude is reduced by $\sqrt{2}$ and the corresponding initial velocity v_0, Eq. (3), is the same as in the two-dimensional simulation, and;
2. $a_0^- = 0.29$ cm, such that the preshock amplitude is the same as in the two-dimensional simulations and the corresponding value of v_0 is $\sqrt{2}$ larger than in the two-dimensional case.

A summary of these initial conditions, including a comparison to the two-dimensional mix initial conditions is presented

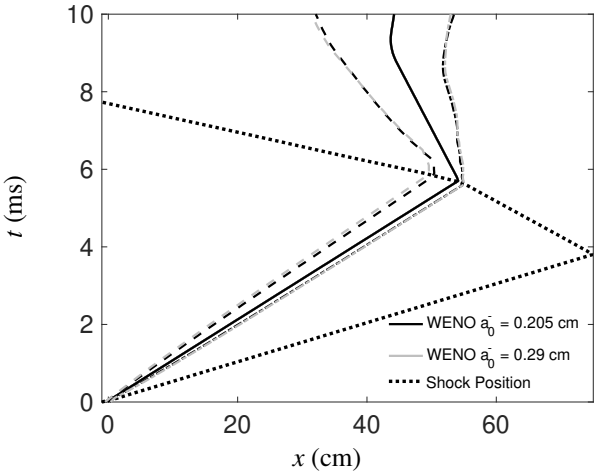

Figure 13: The x-t diagram showing the position of the interface $\ell_{\rm int}(t)$ (solid line), shock (dotted line), and bubble and spike locations $\ell_b(t)$ and $\ell_s(t)$ (dash-dot and dashed lines, respectively) for the three-dimensional simulation with $a_0^- = 0.205$ cm and $a_0^- = 0.29$ cm.

in Table 6. The simulations were performed using the ninth-order WENO method with a resolution of 128 points per initial perturbation wavelength (as compared to 512 points for the two-dimensional simulation). Symmetry boundary conditions were used in the transverse directions.

The location of the left boundary for L_x and L_y may appear arbitrary. The reason for this choice is that the code places the mesh point at the center of the cell. Therefore, the selection of the limits corresponds to the first grid point at -3 cm for L_x and at 0 cm for L_y. The right side limit is obtained by multiplying the number of grid points N by the grid spacing Δx. This ensures that, as the grid spacing is halved and the number of grid points is increased, the grid points overlap.

Figure 13 shows a comparison of the x-t diagram for the three-dimensional simulations with $a_0^- = 0.205$ and 0.29 cm, including the bubble and spike position, unperturbed interface position, and the shock position. Prior to reshock, the spike position from the simulation with $a_0^- = 0.29$ cm is slightly behind that of the simulation with $a_0^- = 0.205$. The bubble positions are the same. The location of the shock and the time of reshock are the same. Following reshock, differences between the two simulations become less evident. In particular, the positions for both the bubble and spike agree well, even following the arrival of the reflected rarefaction at ≈ 8.5 ms.

6.2. *Baroclinic circulation deposition on the interface and comparison to linear theory*

The circulation on the sinusoidal interface is defined by generalizing Eq. (13) to three dimensions:

$$\langle \omega_i \rangle (y, z, t) = \int_{-\infty}^{\infty} \omega_i(x, y, z, t)\, \mathrm{d}x\,. \tag{39}$$

Equation (39) can be compared with the predictions of linear theory [61]. By analogy with two dimensions, define the vortex dipole in three dimensions

$$\mu(x, y) = 2\, v_0 \cos\left(k_x\, x\right) \cos\left(k_y\, y\right), \tag{40}$$

so that the initial vortex sheet in three dimensions is

$$\boldsymbol{\gamma}(x, y) = \frac{\frac{\partial \mu}{\partial y}\widehat{\boldsymbol{i}} - \frac{\partial \mu}{\partial x}\widehat{\boldsymbol{j}} + \left(\frac{\partial \eta}{\partial x}\frac{\partial \mu}{\partial y} - \frac{\partial \eta}{\partial y}\frac{\partial \mu}{\partial x}\right)\widehat{\boldsymbol{k}}}{\sqrt{1 + \left(\frac{\partial \eta}{\partial x}\right)^2 + \left(\frac{\partial \eta}{\partial y}\right)^2}}\,. \tag{41}$$

For the present η [Eq. (37)] and μ [Eq. (40)], it follows that $\gamma_3 \equiv 0$.

Figure 14 shows a visualization of the initial baroclinic circulation deposition by the shock for the $a_0^- = 0.205$ cm initial condition. The right column shows surface plot visualizations for the simulations with a comparison to the predictions of linear theory. The first column shows $\langle \omega_1 \rangle (y, z, 0^+)$, $\langle \omega_2 \rangle (y, z, 0^+)$, and $\langle \omega_3 \rangle (y, z, 0^+)$ used to visualize the initial baroclinic circulation deposition on the interface by the shock and a visualization of the initial enstrophy on the interface $\langle \Omega \rangle (y, z, 0^+)$, where

$$\Omega(x, y, z, t) = \frac{\omega_1^2 + \omega_2^2 + \omega_3^2}{2} \tag{42}$$

is the enstrophy. The isosurface is computed at a value corresponding to half the maximum and minimum enstrophy values. A uniform layer of enstrophy is deposited on the interface and white represents regions where $\Omega = 0$, corresponding to the tip of the bubble or the tip of the spike. An (x, y)-cross-section corresponding to $z_{\rm mid}$ shows the deposition of enstrophy on the interface and the zero values of the enstrophy corresponding to the tip and bottom of the bubble. The enstrophy is expected to be zero in these regions, just as the vorticity is zero at the tip of the bubble and spike. In these regions the density and pressure gradients are parallel, so that the baroclinic vorticity production vanishes.

The values of $\langle \omega_1 \rangle (y, z, 0^+)$ are much smaller than the values for the other components of the vorticity field, indicating that it is negligible; $\langle \omega_2 \rangle (y, z, 0^+)$ and $\langle \omega_3 \rangle (y, z, 0^+)$ show the formation of alternating strong positive and negative vortices, as expected by the different misalignments of the density and pressure gradient vectors. Note that $\langle \omega_3 \rangle (y, z, 0^+)$ is the same as $\langle \omega_2 \rangle (y, z, 0^+)$, but rotated 90° clockwise. The second column shows the predictions for $\langle \omega_2 \rangle (y, z, 0^+)$ and $\langle \omega_3 \rangle (y, z, 0^+)$ from linear theory. Linear theory gives similar qualitative and quantitative predictions as those from the simulations. The only difference is that the maximum values are slightly larger in the linear prediction, and that the vortices are much rounder in the linear predictions. The discrepancy can be attributed to the fact that the simulation values are measured at 0.06 ms, so that the circulation deposited on the interface by the shock has evolved. The surface plots for $\langle \omega_1 \rangle (y, z, 0^+)$ show a disordered noisy structure, while the surface plots of $\langle \omega_2 \rangle (y, z, 0^+)$ and $\langle \omega_3 \rangle (y, z, 0^+)$ show the formation of a sinusoid-like structure with the prediction of linear theory shown above the simulation in the peaks of the vortices and shown below in the case of the valleys. A visualization for the $a_0^- = 0.29$ cm initial condition yields similar results and is not shown.

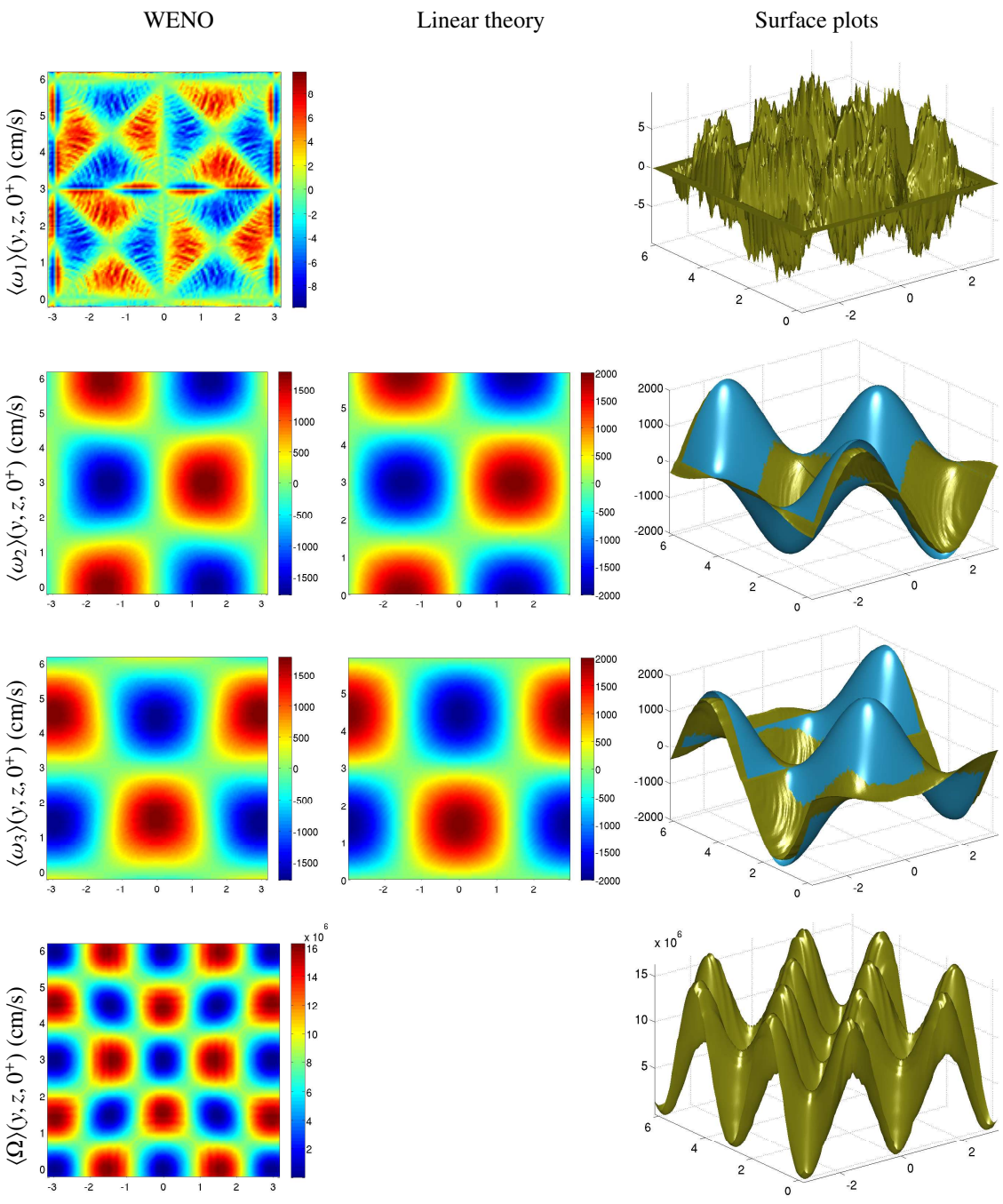

Figure 14: The initial circulation deposition on the interface from the three-dimensional WENO simulation with $a_0^- = 0.205$ cm, as measured by the averaged components of the vorticity vector $\langle\omega_1\rangle(y,z,0^+)$, $\langle\omega_2\rangle(y,z,0^+)$, $\langle\omega_3\rangle(y,z,0^+)$, and the enstrophy $\langle\Omega\rangle(y,z,0^+)$ from the incident shock at time 0^+ (left column) with the comparison from linear instability theory (center column). Also shown is the surface-plot comparison of the results from the simulation (green) with the results from linear instability theory (blue) (right column).

	3D $a_0^- = 0.205$ cm initial conditions		3D $a_0^- = 0.29$ cm initial conditions		2D mix initial conditions	
k (cm^{-1})	1.4976		1.4976		1.0590	
v_0 (cm/s)	1336.8		1891.2		1336.8	
	Preshock	Postshock	Preshock	Postshock	Preshock	Postshock
a_0 (cm)	0.205	0.1513	0.29	0.214	0.29	0.214

	3D Numerical parameters		2D Numerical parameters	
	x	y and z	x	y
N	1683	129	6726	513
L (cm)	$[-3.0232, 75.0216]$	$[-0.0232, 5.9624]$	$[-3.0058, 75.0042]$	$[-0.0058, 5.9334]$
Δx (cm)	0.0464	0.0464	0.0116	0.0116

Table 6: Initial conditions for the three-dimensional simulations and a comparison to those for the two-dimensional simulation.

	3D $a_0^- = 0.205$ cm initial conditions		3D $a_0^- = 0.29$ cm initial conditions	
	WENO	Theory	WENO	Theory
$\max\left[\langle\omega_1\rangle(y,z,0^+)\right]$ (cm/s)	9.7698	0	20.8719	0
$\max\left[\langle\omega_2\rangle(y,z,0^+)\right]$ (cm/s)	1.7828×10^3	1.9525×10^3	2.5768×10^3	2.7623×10^3
$\max\left[\langle\omega_3\rangle(y,z,0^+)\right]$ (cm/s)	1.7835×10^3	1.9525×10^3	2.5765×10^3	2.7623×10^3
$\max\left[\langle\Omega\rangle(y,z,0^+)\right]$ (cm/s^2)	1.6267×10^7	–	3.2774×10^7	–

Table 7: Comparison of the initial circulation deposition $\max\left[\langle\omega_1\rangle(y,z,0^+)\right]$, $\max\left[\langle\omega_2\rangle(y,z,0^+)\right]$, and $\max\left[\langle\omega_3\rangle(y,z,0^+)\right]$ from the three-dimensional simulations with $a_0^- = 0.205$ and 0.29 cm together with the predictions of linear instability theory. Also shown is the baroclinic circulation deposition on the interface $\max\left[\langle\Omega\rangle(y,z,0^+)\right]$.

A quantitative measure of the initial circulation deposition is obtained by comparing the maximum values from the WENO simulations with the predictions of linear theory. The results for the simulations with $a_0^- = 0.205$ and 0.29 cm are given in Table 7, and indicate that linear theory overpredicts the simulation by 8.7% for $a_0^- = 0.205$ cm and by 2.5% for $a_0^- = 0.29$ cm. The values of ω_3 and ω_2 also confirm that the simulations retain symmetry, as the difference is only 0.04%. The results also show that the simulation with $a_0^- = 0.29$ cm has initial circulations that are one third larger than those with $a_0^- = 0.205$ cm. The nonzero value of $\max\left[\langle\omega_1\rangle(y,z,0^+)\right]$ indicates an error of 1% between the simulations and theory. As the simulation values are taken at 0.06 ms, the baroclinic vorticity production has already modified the vorticity, which can be quantified as follows. The baroclinic vorticity production has magnitude $\mathcal{P}_1 \sim \times 10^7$ and $\mathcal{P}_2 \sim 10^9$ s^{-2} in the streamwise (x) and periodic (y and z) directions, respectively. For $\Delta t \sim 0.06$ ms, this corresponds to an increase in vorticity $\Delta\langle\omega_1\rangle \sim \Delta t\,\mathcal{P}_1 \sim 6 \times 10^2$ and $\Delta\langle\omega_2\rangle \sim \Delta t\,\mathcal{P}_2 \sim 6 \times 10^4$ s^{-1}, which is consistent with the discrepancy between the WENO results and the predictions from linear instability theory.

6.3. Dynamics of the instability evolution

Presented here is a visualization of the time-evolution of the Richtmyer–Meshkov instability in three dimensions using the mass fraction and enstrophy isosurfaces. As the initial surface in three-dimensions (37) is a product of sine waves, a distinctive "bubble" corresponding to the perturbation entering into the SF_6, and a distinctive "spike" corresponding to the perturbation entering into the air(acetone) can be identified. In addition, a "front side" corresponding to a view from the air(acetone) side, and a "back side" corresponding to a view from the SF_6 side can be identified. The visualizations shown are for the $a_0^- = 0.205$ cm initial condition (the visualizations for $a_0^- = 0.29$ cm are expected to be very similar and are not shown).

Figure 15 shows the time-evolution of the mass fraction isosurfaces illustrating the dynamics of the bubble and spike from the front air(acetone) side and the back (SF_6) side from the WENO simulation. The first row shows the mass fraction isosurface corresponding to $m_{SF_6} = 1/2$: "spike front" denotes a view of the isosurface from the air(acetone) side; "bubble back" denotes a view from the SF_6 side. The isosurfaces show the shocked initial sinusoidal interface. Also shown is the (x, y)-cross-section corresponding to the central value of the z-coordinate z_{mid}.

The bubble front contains a quarter of the spike front corresponding to the sides on the quarters, which becomes more apparent at later times. Following the passage of the shock, bubbles of air(acetone) start penetrating into the heavier SF_6 and spikes of SF_6 start penetrating into the air(acetone). At 1.16 ms, a tube-like feature links the spike fronts at the separation between the bubbles and the spikes: this feature is the result of the initial conditions and the fact that in three dimensions two roll-ups are observed, one corresponding to the spike and one to the bubble. These tube-like features form the roll-up of the bubble and spike at 1.76 ms. On the front bubble, features appear

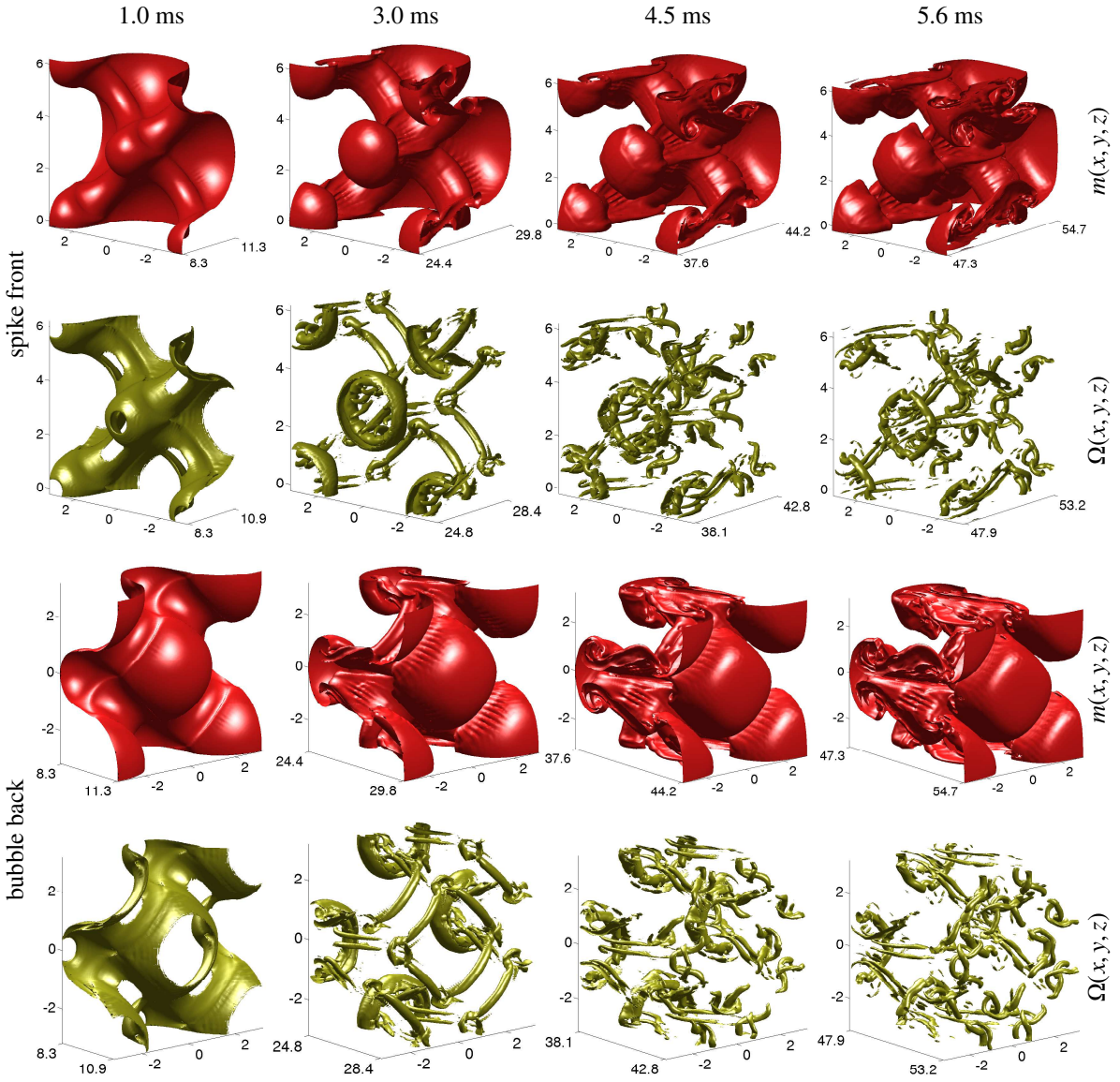

Figure 15: Time-evolution of the mass fraction isosurface $m_{SF_6} = 1/2$ and enstrophy isosurface $\Omega = 10^8$ s^{-2} at 1.0, 3.0, 4.5, and 5.6 ms from the WENO simulation. The spike side facing the air(acetone) (top two rows), and the bubble side facing SF_6 (bottom two rows) are shown.

at the corners due to the interaction of the bubble with adjacent bubbles, indicating the onset of the nonlinear interaction. As the instability develops further, the bubble and spike roll-up further. At 3.0 ms, the spike develops a further structure on the roll-up. This structure can be seen when visualizing the back of the spike, where corrugations form on the curved part of the spike. This structure is further evident at 4.5 ms when these additional structures can be seen on both the front and back of the spike, and develop a nearly star-shaped feature. At late times (5.6 ms) the roll-ups develop additional complex structure. The sides of the mass fraction isosurface offer a view of the roll-ups, which are similar to those in the two-dimensional simulation.

Figure 15 also shows the time-evolution of the enstrophy isosurfaces following the passage of the shock through 5.6 ms. The enstrophy [Eq. (42)] is used here to visualize the dynamics of the vorticity. Immediately following the passage of the shock at 0.06 ms, a layer of vorticity is deposited on the interface by the baroclinic vorticity production mechanism. At 1.0 ms, the enstrophy isosurfaces begin rolling up with bubbles of air(acetone) penetrating into the SF_6 and spikes of SF_6 penetrating into the air(acetone). At 3.0 ms, the enstrophy shows a toroidal tube-like structure indicating the formation of a rotating vortex corresponding to the spike. The bubble also shows a similar circular feature but is larger. In the simulation, the vortex tubes meet at corners forming a complex structure. In addition, ripples in the mass fraction isosurface are observed at 3.0 ms, which may be due to instabilities developing at the bubble surface. In addition, the vortex tubes connecting the spike to the bubble divide, indicating that further roll-ups are occurring. The bubble also shows the formation of complex structures. The enstrophy isosurface shows the formation of a toroidal structure in the bubble core where the roll-up develops. At 4.5 ms, this toroidal structure fragments. At later times, the spike still retains a dominant central core, while the bubble fragments further. The vortex tubes also become smaller with the formation of thinner and finer structures. This is the result of vortex stretching at the interface which causes the elongation of the vortex tubes (an effect absent in two dimensions due to the absence of vortex stretching).

6.4. Comparison of the perturbation, bubble, and spike amplitudes to the predictions of an amplitude growth model

Figure 16 shows a comparison of the perturbation amplitudes $a(t)$ from the three-dimensional simulations with $a_0^- = 0.29$ and 0.205 cm with those from the two-dimensional simulation and the experimental data. The amplitudes from the three-dimensional simulations overpredict the two-dimensional results. The three-dimensional simulation with $a_0^- = 0.205$ cm is in best agreement with the two-dimensional results (due to the matching initial velocity v_0 prior to reshock) and with the experimental data. The amplitudes from the three-dimensional simulations are in excellent agreement for both initial conditions after reshock. Also shown is a comparison of the bubble and spike amplitudes $a_b(t)$ and $a_s(t)$. Whereas the bubble amplitudes from the two three-dimensional simulations agree well, the spike amplitude from the $a_0^- = 0.29$ cm simulation is much larger.

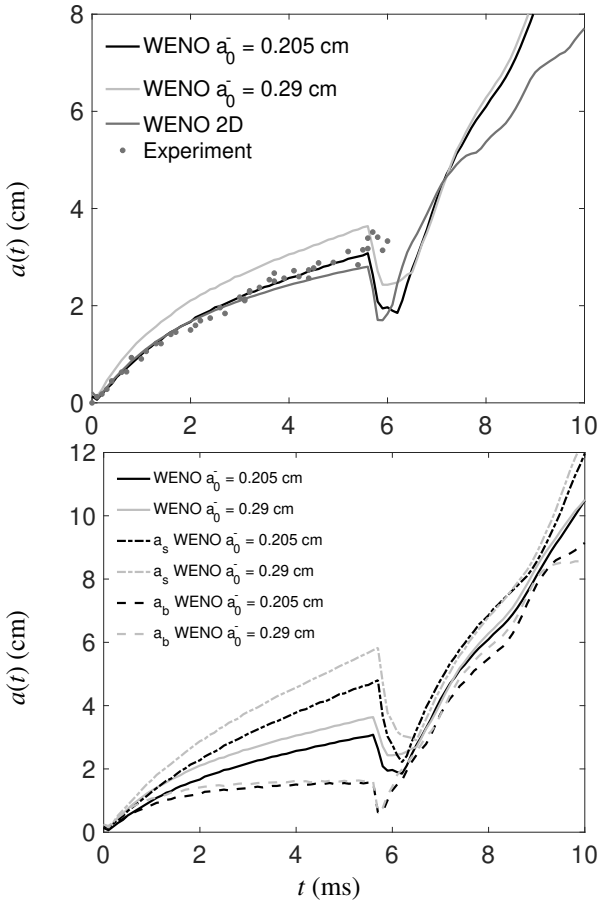

Figure 16: Comparison of the perturbation amplitude $a(t)$ from the simulations with $a_0^- = 0.205$ and 0.29 cm with the two-dimensional simulation and experimental results (top). The corresponding bubble and spike amplitudes $a_b(t)$ and $a_s(t)$ are also shown (bottom).

Figure 17 show a comparison of the WENO perturbation amplitudes and the predictions of the three-dimensional Zhang–Sohn model [59]

$$\frac{\mathrm{d}a}{\mathrm{d}t} = \frac{v_0}{1 + \epsilon\, a_0^+\, v_0\, \lambda_1\, t + \max\left[0, \left(k\, a_0^+\, \lambda_1\right)^2 - \lambda_2\right](k\, v_0\, t)^2}, \quad (43)$$

where $\lambda_1 = 0.08887\,(At^+)^2 + 0.45567$ and $\lambda_2 = 0.39136\,(At^+)^2 + 0.22784$. The Zhang–Sohn model prediction agrees with the simulation amplitudes at early-to-intermediate times. At later times, the models underpredict the simulation amplitudes.

Figure 17 also shows a comparison of $a_b(t) - a_b(0^+)$ from the WENO simulations with the predictions of the Zhang–Sohn model

$$\frac{\mathrm{d}a_b}{\mathrm{d}t} = -\frac{\mathrm{d}a}{\mathrm{d}t} + \frac{k\, v_0^2\, \lambda_3\, t}{1 + \frac{k^2\, a_0^+\, v_0\, \lambda_4}{\lambda_3} + \left[\left(\frac{k\, a_0^+\, \lambda_4}{\lambda_3}\right)^2 + \frac{\lambda_5}{\lambda_3}\right](k\, v_0\, t)^2}, \quad (44)$$

where $\lambda_3 = 4.8482\,(At^+)^3 + 1.8257 At^+$, $\lambda_4 = 0.32772\,(At^+)^3 + 9.87594 At^+$, and $\lambda_5 = 0.02435\,(At^+)^3 + 3.15422 At^+$. The predicted bubble amplitude agrees with the simulated bubble am-

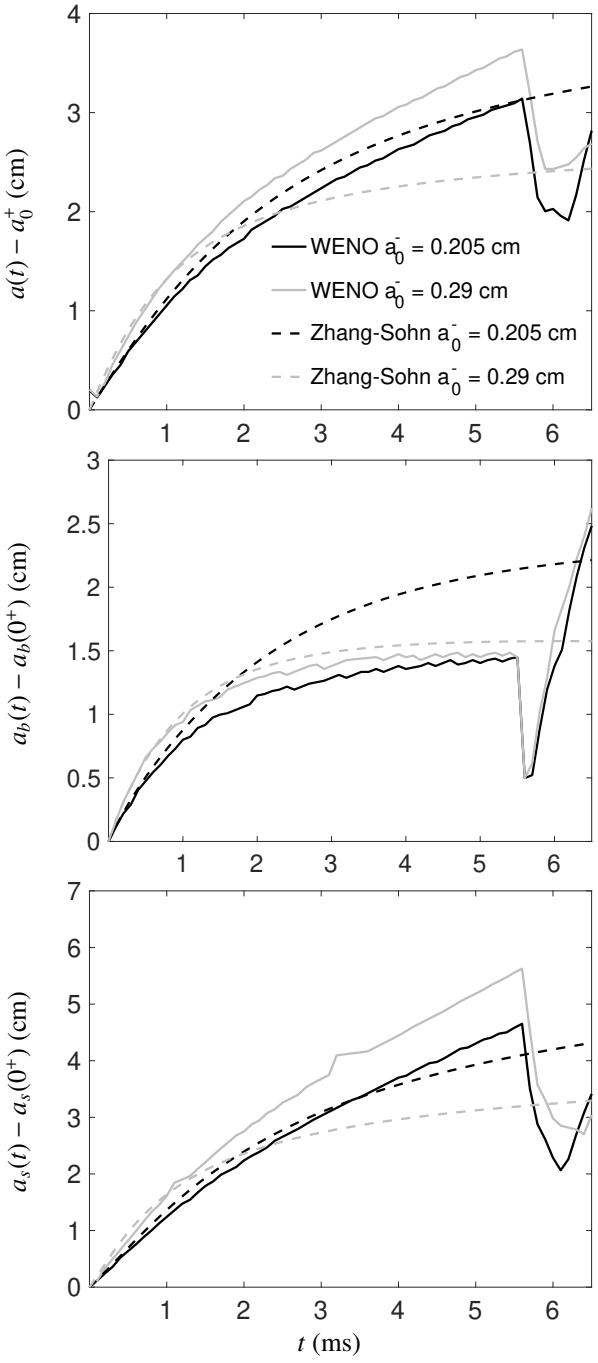

Figure 17: Comparison of the perturbation amplitudes $a(t) - a_0^+$ (top), $a_b(t) - a_b(0^+)$ (middle), and $a_s(t) - a_s(0^+)$ (bottom) from the WENO simulations with $a_0^- = 0.205$ and 0.29 cm with the predictions of the Zhang–Sohn model.

	$a_0^- = 0.205$ cm	$a_0^- = 0.29$ cm
	Δ_{sim}	Δ_{sim}
Zhang–Sohn Padé (all)	5.9	36.2
Zhang–Sohn Padé (bubble)	15.4	5.5
Zhang–Sohn Padé (spike)	5.47	35.4

Table 8: Average fractional deviation Δ_{sim} between the simulation amplitudes for $a_0^- = 0.205$ and 0.29 cm and the predictions of the Zhang–Sohn model.

plitudes at early times. At later times, the model underpredicts the simulation amplitudes.

Also shown in Fig. 17 is a comparison of $a_s(t) - a_s(0^+)$ from the simulations with the predictions of the Zhang–Sohn model

$$\frac{\mathrm{d}a_s}{\mathrm{d}t} = \frac{\mathrm{d}a}{\mathrm{d}t} + \frac{k\, v_0^2\, \lambda_3\, t}{1 + \frac{k^2\, a_0^+\, v_0\, \lambda_4}{\lambda_3} + \left[\left(\frac{k\, a_0^+\, \lambda_4}{\lambda_3}\right)^2 + \frac{\lambda_5}{\lambda_3}\right](k\, v_0\, t)^2}\,. \tag{45}$$

The model predictions agree with the simulation spike amplitude at early times. At late times, the models underpredict the simulation amplitude. The agreement between the model predictions and the simulation amplitudes can be made quantitative by computing the average fractional deviation Δ_{sim} (30) shown in Table 8.

6.5. Dynamics of the reshock process

As in the analysis of the two-dimensional case in Sec. 5, the transmitted shock reflects from the end wall of the shock tube and interacts with the evolving mixing layer during reshock at $\approx$ 5.65 ms. Investigated here are the dynamics of reshock in three dimensions, including a visualization of the complex wave interactions. The mixing layer amplitude is also compared to the predictions of the reshock models considered in Sec. 5.2 for the two-dimensional case.

Figures 18–20 show the dynamics of the mass fraction isosurface, including the arrival of the shock wave (5.7 ms), the inversion process (5.8 and 5.9 ms), and the development of a complex mixing layer at late times (8 and 10 ms). At 5.7 ms, reshock is indicated by the compression of the bubble which now shows a flat tip. Following reshock, a transmitted shock enters the air(acetone) and a reflected rarefaction returns into the SF_6. The vorticity deposited by reshock induces an inversion process, where the bubble turns into a spike and vice versa. The inversion process at 5.8 and 5.9 ms shows the bubble returning back into the air(acetone). The spike is also compressed by the passage of the transmitted shock, causing the formation of additional complex structures in the roll-up. At 6.0 ms (see Fig. 19), the mixing layer is compressed and shows the formation of complex structures. At 6.5 ms, the new spike generated by the inversion of the bubble forms. This spike grows at later times (7, 8, and 10 ms), as shown in Fig. 20. This central spike is the only large-scale structure following reshock, and is similar to that in the two-dimensional simulation shown in Fig. 9.

Figures 18–20 also show the time-evolution of the mass fraction isosurface during reshock. At 5.7 ms, reshock causes a significant deposition of vorticity on the interface. As a result, the

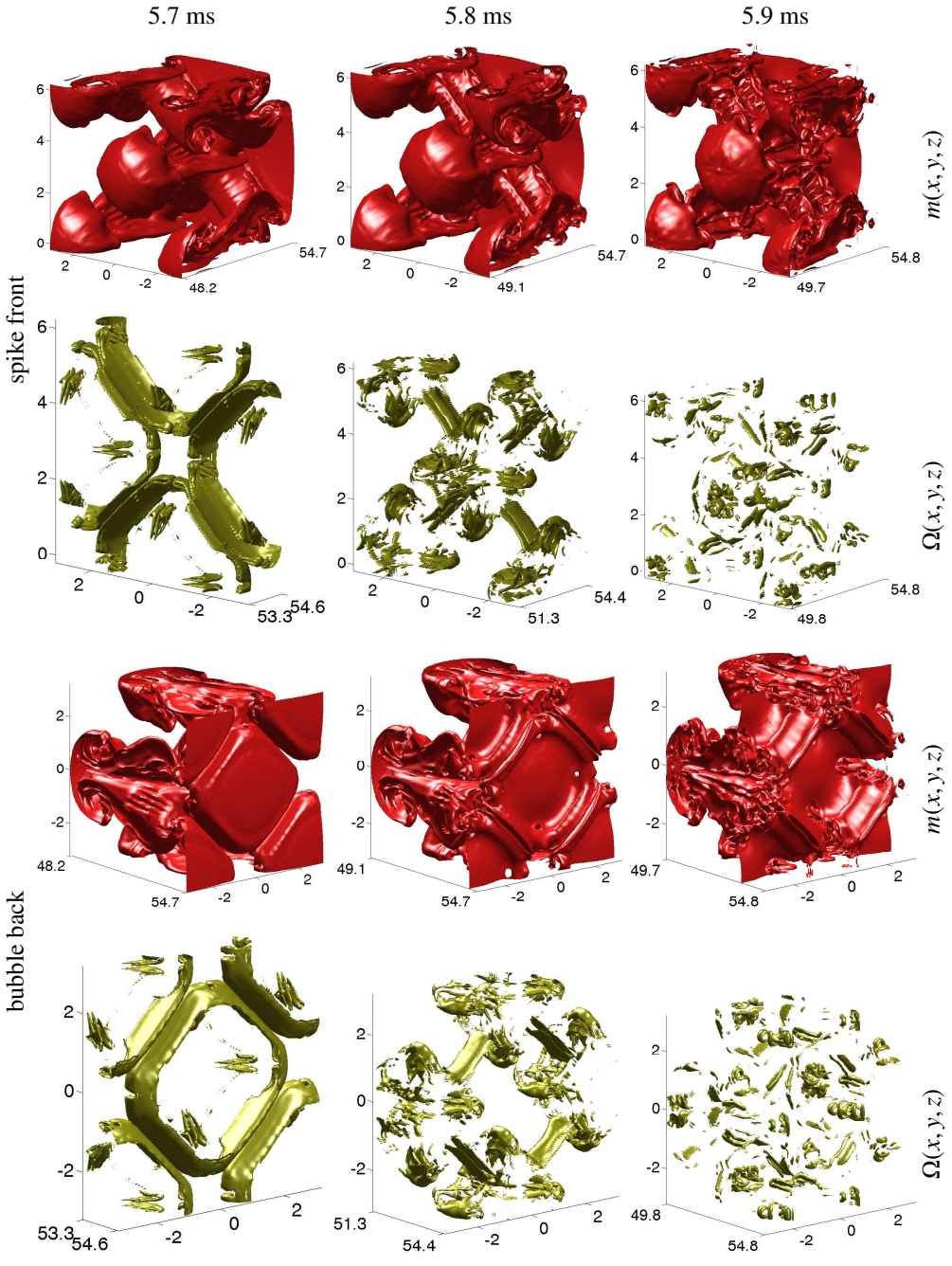

Figure 18: Time-evolution of the mass fraction isosurface $m_{SF_6} = 1/2$ and enstrophy isosurface $\Omega = 10^8$ s^{-2} at 5.7, 5.8, and 5.9 ms from the WENO simulation. The spike side facing the air(acetone) (top two rows) and the bubble side facing SF_6 (bottom two rows) are shown.

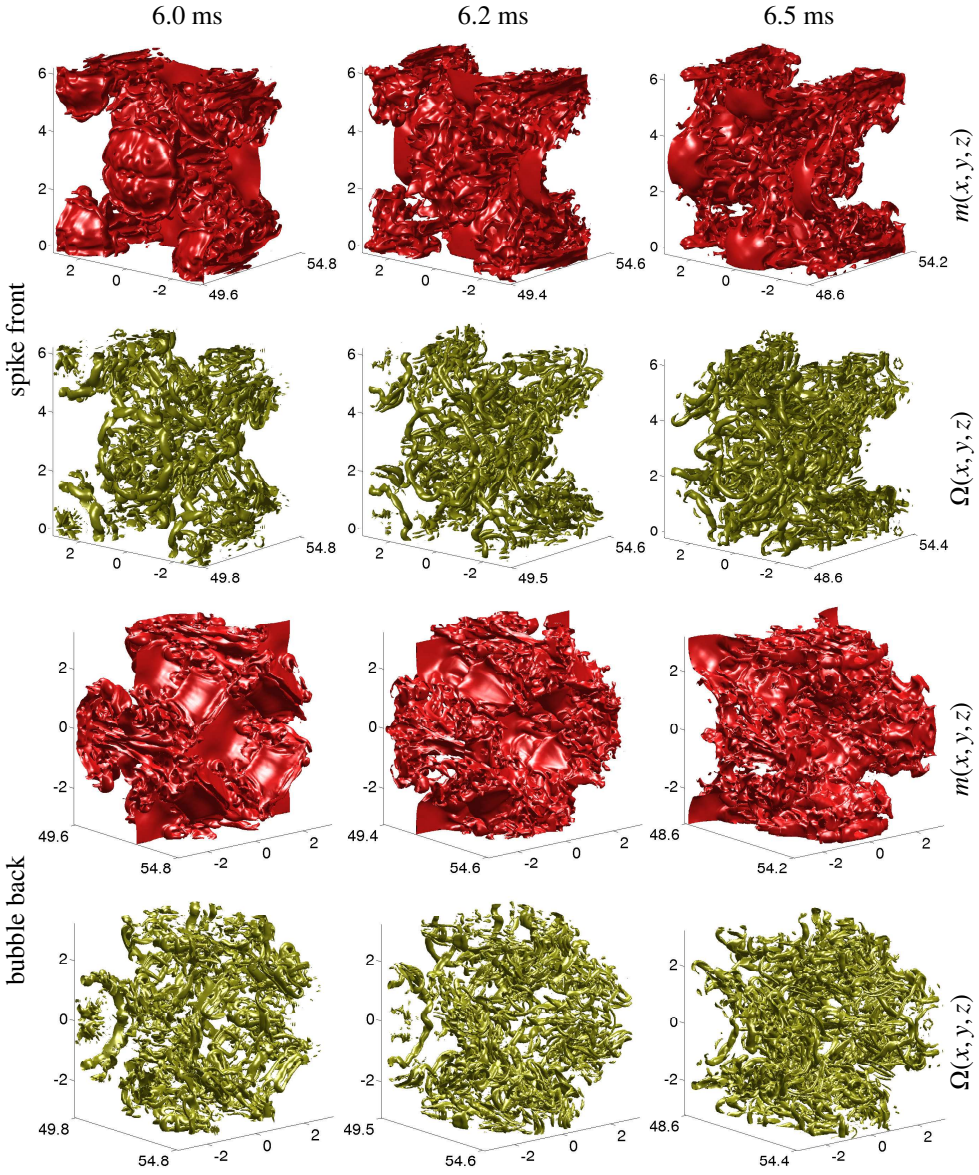

Figure 19: Same as Fig. 18 but at 6.0, 6.2, and 6.5 ms.

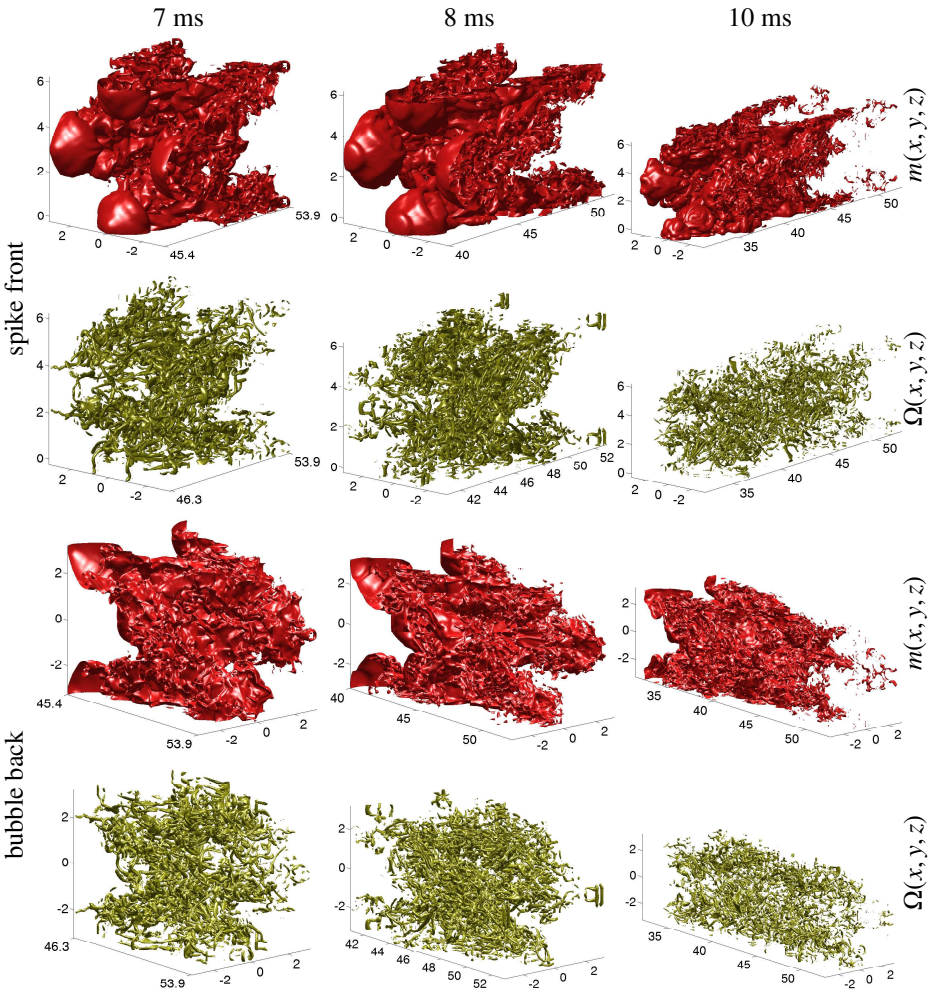

Figure 20: Same as Fig. 18 but at 7, 8, and 10 ms.

enstrophy is largest at reshock and the isosurface only shows a structure corresponding to the reshocked surface. Furthermore, as the vorticity is generated by the misalignment of the density and pressure gradients, it attains its largest values near the curved parts of the bubble. This explains why the enstrophy isosurface is primarily observed along a strip on the side of the bubble. At 5.8 ms, the transmitted shock has interacted with the spike, causing deposition of vorticity in the region. At 5.9 ms, the vorticity begins fragmenting. This fragmentation continues with the formation of a dense, thick, tubular structure by 6 ms in Fig. 19. This phenomenon is further observed at 6.2 and 6.5 ms. At later times, the mixing layer width grows, but the fragmentation of the vorticity persists, forming complex structure.

Figures 21 and 22 show the density cross-sections for the bubble and spike during reshock. At 5.7 ms, the transmitted shock enters the air(acetone) and a reflected rarefaction wave returns into the SF_6. The reflected rarefaction is clearly visible from the lighter red colors corresponding to the bubble position. The transmitted shock is weaker and is visible only when it interacts with the spike, where it leaves behind a dark red color. The transmitted shock is not seen in the air(acetone), as it is weak and does not significantly increase the density. The transmitted shock enters the spike at 5.8 ms and the interactions with the density structures cause the formation of a complex system of reflected and transmitted waves. At 5.9 ms, the transmitted shock has crossed the mixing layer and the inversion process begins.

The visualizations at 6.0, 6.1, 6.3, and 6.5 ms show the inversion process, with the pre-reshock spike thinning and the pre-reshock bubble transforming into a strong spike. At 7 ms, this spike begins to roll-up as shown in Fig. 22. A reflected rarefaction wave further interacts with the mixing layer after 8 ms and causes the change in colors at 10 ms. Between the spikes, the density cross-sections reveal the formation of a well-mixed region as also observed in the two-dimensional simulation (see Fig. 11). However, whereas the two-dimensional simulation exhibits the formation of strong vorticity cores, the enstrophy isosurface shows that the vorticity is fragmented and forms small, short, tubular structures in three dimensions. The differences between the two- and three-dimensional cases is again attributable to the absence of vortex stretching in two dimensions (in which coherency of the flow structures persists).

The mixing layer amplitude after reshock is compared to the predictions of the reshock models considered for the two-dimensional simulation in Sec. 5.2. As the models for the mixing layer amplitude are linear, the velocity can be computed in dimensional and rescaled units (see Table 9). Figure 23 shows a comparison of the mixing layer amplitude from the three-dimensional WENO simulations with $a_0^- = 0.205$ and 0.29 cm, together with the prediction of the Mikaelian model (33), the Brouillette–Sturtevant model (34), the Charakhch'yan model (35), and the Lombardini et al. model (36). The Mikaelian model depends only on the post-reshock Atwood number At_1^+, which has the same value in both simulations: as a result, only a single curve is plotted. This model overpredicts the numerical results. By contrast, the Brouillette–Sturtevant model yields a different prediction for each simulation. The prediction corresponding to $a_0^- = 0.205$ cm has the smallest value, followed by the model corresponding to $a_0^- = 0.29$ cm (30% larger), as given in Table 9. The Charakhch'yan model depends on the post-reshock Atwood number At_1^+ and the Richtmyer velocity v_0, so that two curves are plotted corresponding to the simulations with the two initial amplitudes. This model gives the smallest prediction for $a_0^- = 0.205$ cm, and the prediction for $a_0^- = 0.29$ cm is 30% larger. The Lombardini et al. model prediction is quite close to that of the Mikaelian model. In conclusion, the predictions of the Mikaelian reshock model are in best overall agreement with the present simulation results, as the post-reshock mixing layer amplitude does not depend on the pre-reshock amplitude.

7. Summary and Conclusions

The ninth-order WENO shock-capturing method was applied to simulate a model of the Mach 1.3 air(acetone) and SF_6 Jacobs and Krivets single-mode Richtmyer–Meshkov instability experiment [15] extended numerically to include reshock. In this experiment, the larger Mach number compared to previous studies allowed the investigation of late-time effects prior to the arrival of the transmitted shock in the reshock phase. The present study analyzed the development of the instability prior to reshock, during the reshock phase, and post-reshock. As with all other shock-capturing methods, at most first-order accuracy can be achieved in the postshock region [62, 63]. Despite the loss of accuracy, high-order shock-capturing methods are desirable for the accurate evolution of high-frequency components and small-scale structure [64] present in the complex mixing layer of Richtmyer–Meshkov instability, and for the reduced numerical dissipation associated with higher-order flux reconstructions and finer grids [22].

In the WENO simulations, a single value of the adiabatic exponent γ was specified corresponding to a mixture of 50% air(acetone) and 50% SF_6 using mix initial conditions. The incident shock Mach number was therefore very slightly increased so that the initial velocity v_0 matched that in the experiment. Excellent agreement was found between the vorticity deposited on the interface in the simulations compared to the predictions of the Samtaney–Zabusky circulation-deposition model and linear instability theory. A comparison of the density fields from the WENO simulations with the experimental PLIF images showed good agreement in the large-scale structures but differences in the small-scale structures. In particular, the WENO and PLIF images showed similar small-scale structure within the roll-ups.

The perturbation amplitude from the two-dimensional simulation was in generally good agreement with the experimental data points. The perturbation, bubble, and spike amplitudes from the simulation were compared with the predictions of several nonlinear amplitude growth models, where the growth was reduced to account for the diffuse initial interface. In general, the model predictions agreed with the simulation amplitudes at early-to-intermediate times ($\tau < 4$) and underpredicted the amplitudes at later times, corresponding to the late nonlinear

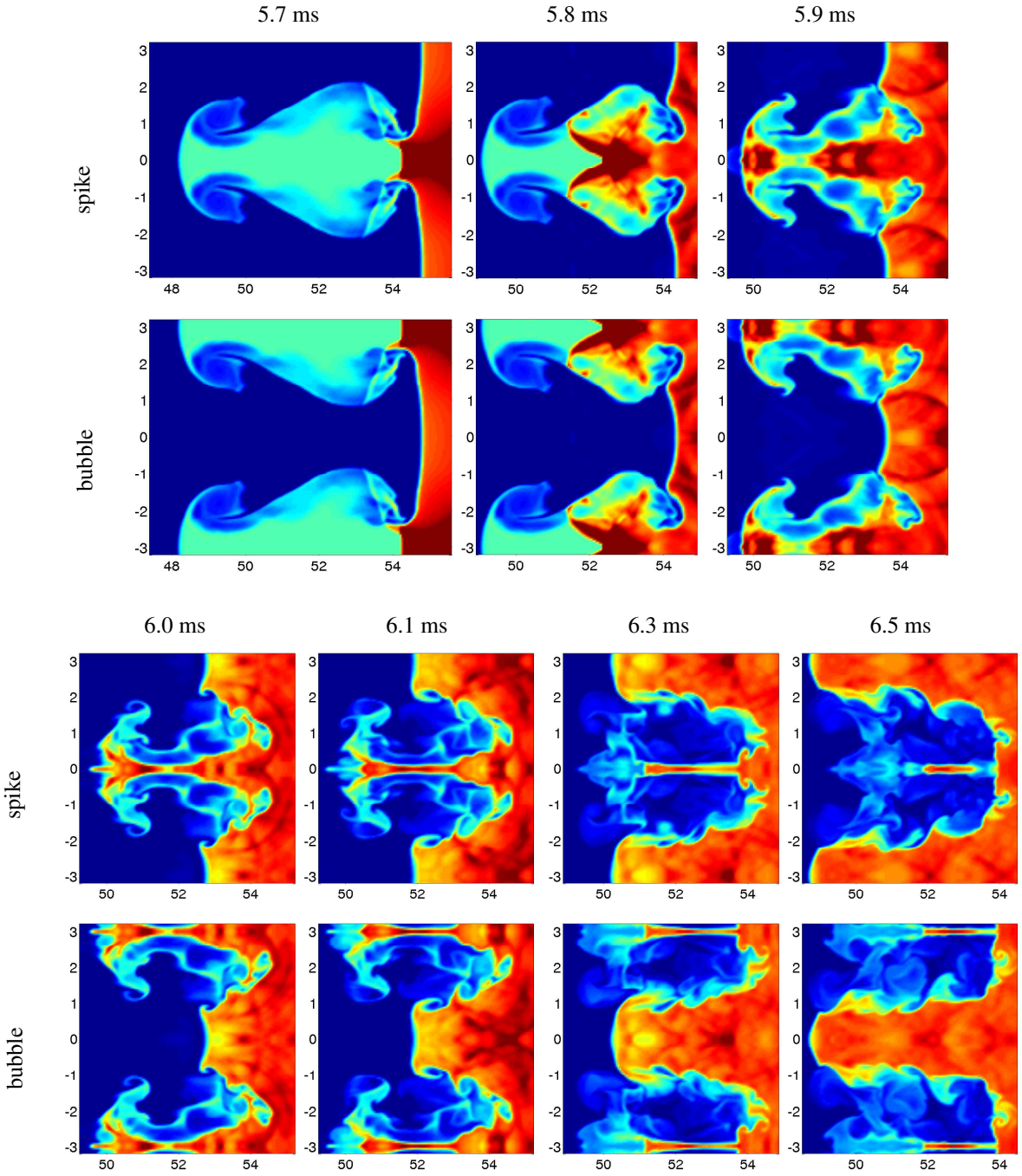

Figure 21: Time-evolution of the density in the (x, y)-plane at 5.7, 5.8, 5.9, 6.0, 6.1, 6.3, and 6.5 ms from the WENO simulation. Both the evolution of the spike (first and third row) and of the bubble (second and fourth row) are shown.

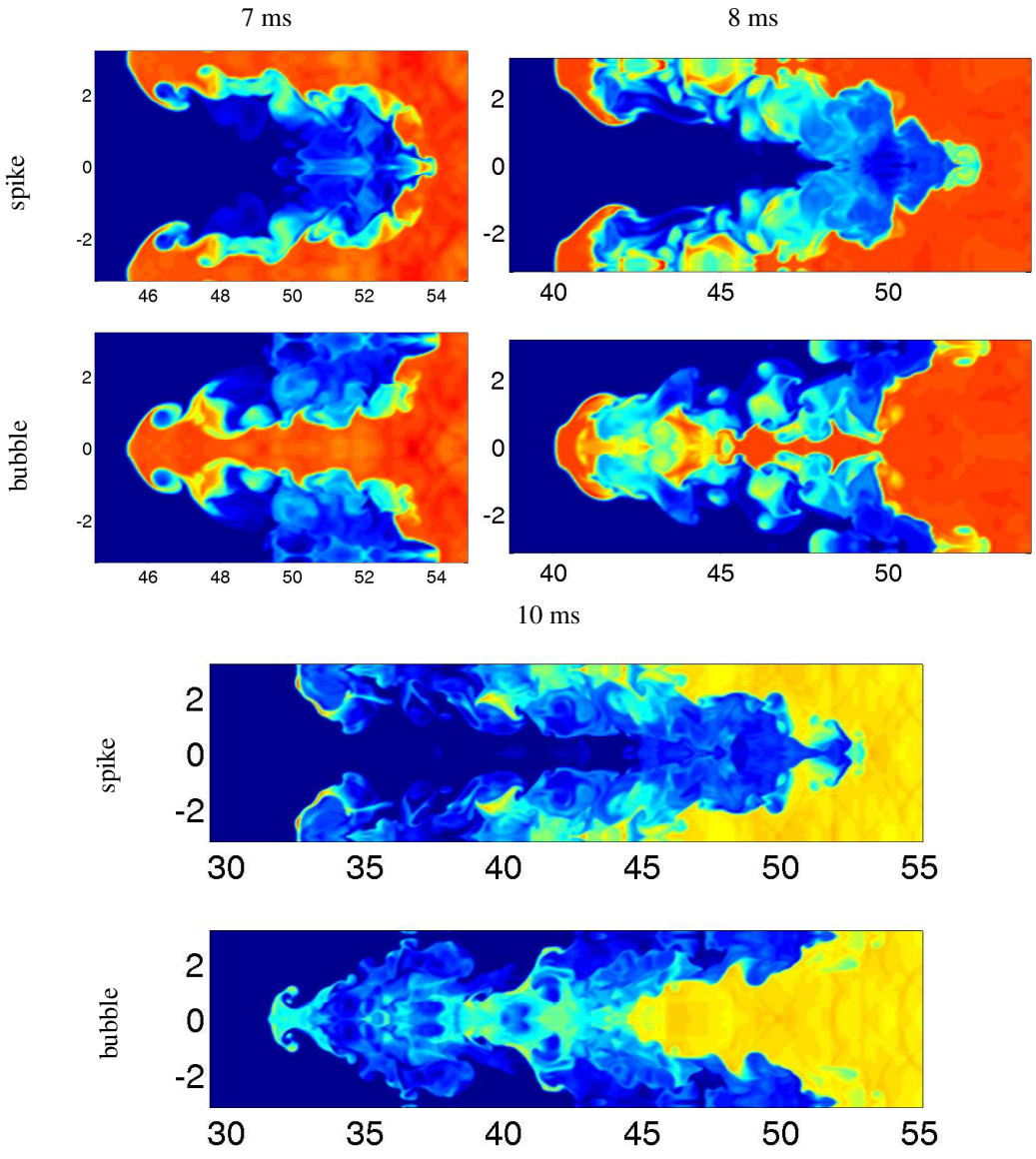

Figure 22: Same as Fig. 21 but at 7, 8 , and 10 ms.

	3D $a_0^- = 0.205$ cm initial conditions		3D $a_0^- = 0.29$ cm initial conditions	
	$\frac{da}{dt}$	$k\frac{da}{d\tau}$	$\frac{da}{dt}$	$k\frac{da}{d\tau}$
Richtmyer	1337	1	1891	1
Mikaelian	3334	2.50	3334	1.76
Brouillette–Sturtevant	3071	2.30	4342	2.30
Charakhch'yan	2534	1.89	3641	1.93
Lombardini et al.	3220	2.41	3220	1.70

Table 9: The velocity da/dt (in units of cm/ms) and the normalized velocity $kda/d\tau$ from the Richtmyer model before reshock for the three-dimensional WENO simulations with $a_0^- = 0.205$ and 0.29 cm. Also shown are the velocities and the normalized velocities from the Mikaelian, Brouillette–Sturtevant, Charakhch'yan, and Lombardini et al. reshock models.

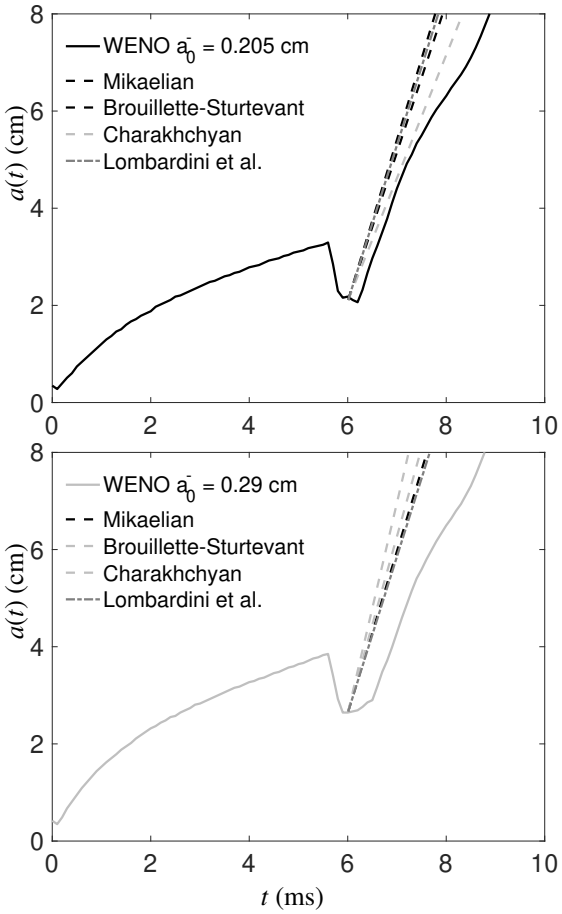

Figure 23: The mixing layer amplitude $a(t)$ from the three-dimensional simulation with $a_0^- = 0.205$ cm (top) and 0.29 cm (bottom), together with the predictions of the Mikaelian, Brouillette–Sturtevant, Charakhch'yan, and Lombardini et al. reshock models.

regime. Overall, the predictions of the Sadot et al. and Zhang–Sohn models were in best agreement with the simulation data. Averaged fractional deviations were computed as metrics quantifying the degree of agreement.

The reshock process was also investigated, which occurs when the transmitted shock reflects from the end wall of the test section and interacts with the evolving mixing layer. Reshock is of fundamental interest as it imparts additional energy into the mixing layer and contributes to the formation of complex disordered structures. Reshock of the interface evolving from a single-mode initial condition generates multimode structures of varying sizes. The postreshock mixing layer width was compared to the predictions of several reshock models and generally good agreement was found between the model predictions and the simulation data. The prediction of the Mikaelian model was in best agreement with the simulation data.

The numerical investigation was also performed in three dimensions where the initial perturbation is a product of sinusoids. Under these initial conditions, the effective wavenumber (which enters into the determination of the velocity v_0) is larger than the corresponding two-dimensional value. Thus, simulations were performed with:

1. initial perturbation amplitude $a_0^- = 0.29$ cm (same as the two dimensional case) resulting in a larger v_0, and;
2. a reduced amplitude $a_0^- = 0.205$ cm (so that v_0 is the same as in two dimensions).

The instability evolution was visualized using the mass fraction isosurface. In three dimensions two roll-ups formed, one corresponding to the spike roll-up (as in two dimensions) and one corresponding to the bubble roll-up. As the spike was compressed and the bubble expanded, the bubble roll-up was larger than the spike roll-up. The vorticity was visualized through the enstrophy isosurface showing the formation of a ring structure corresponding to the cores of the roll-ups and complex structures in the cores.

The perturbation amplitudes from the three-dimensional WENO simulations were compared with those from the two-dimensional simulation and the experimental data. The three-dimensional simulation with $a_0^- = 0.205$ cm was in best agreement with the two-dimensional results and the experimental amplitude data prior to reshock due to the matching initial velocity v_0.

The perturbation amplitudes from the three-dimensional WENO simulations were compared to the predictions of the nonlinear Zhang–Sohn model: although agreement was observed at early times, the model underpredicted the simulation results at later times. In general, overall better agreement between the model and simulations was observed for the $a_0^- = 0.205$ case compared to the $a_0^- = 0.29$ case.

In three dimensions, reshock produced a qualitative change in structures compared to two dimensions. In particular, the enstrophy isosurface showed that the vorticity fragmented and formed small, short, tubular structures in contrast to the two-dimensional vorticity, which formed strong cores. The differences between the two- and three-dimensional dynamics and

structure are directly attributable to the existence of vortex stretching in three dimensions. The mixing layer width from the simulations with different initial perturbation amplitudes were in excellent agreement, indicating that the post-reshock amplitude did not depend on the initial perturbation amplitude. A comparison with the predictions of reshock models showed that the Mikaelian model (which is independent of the pre-reshock amplitude) was in best agreement with the amplitudes following reshock, as also found for the two-dimensional case.

This study indicates that high-order WENO simulations interpreted as implicit large-eddy simulations are useful for investigating the complex fluid dynamics of reshocked Richtmyer–Meshkov instability in two and three dimensions. Comparisons to experimental data (amplitude growth and structure of the density field) indicate favorable agreement. The data from the simulations was also used to quantitatively evaluate the predictions of nonlinear amplitude growth and reshock models. The simulation data elucidated differences between the two- and three-dimensional dynamics, consistent with the expected behavior of the baroclinic vorticity and enstrophy dynamics and vortex stretching mechanism.

Acknowledgments

This work is dedicated to honoring the exemplary scientific career of David L. Youngs. This work was performed under the auspices of the U.S. Department of Energy by Lawrence Livermore National Laboratory under Contract DE-AC52-07NA27344.

This document was prepared as an account of work sponsored by an agency of the United States government. Neither the United States government nor Lawrence Livermore National Security, LLC, nor any of their employees makes any warranty, expressed or implied, or assumes any legal liability or responsibility for the accuracy, completeness, or usefulness of any information, apparatus, product, or process disclosed, or represents that its use would not infringe privately owned rights. Reference herein to any specific commercial product, process, or service by trade name, trademark, manufacturer, or otherwise does not necessarily constitute or imply its endorsement, recommendation, or favoring by the United States government or Lawrence Livermore National Security, LLC. The views and opinions of authors expressed herein do not necessarily state or reflect those of the United States government or Lawrence Livermore National Security, LLC, and shall not be used for advertising or product endorsement purposes.

Appendix A. Numerical Method

The WENO method for the solution of hyperbolic conservation laws is briefly summarized here in one spatial dimension. In the finite-difference WENO method [24], the scalar conservation law

$$\frac{\partial u(x,t)}{\partial t} + \frac{\partial f(u)}{\partial x} = 0 \tag{A.1}$$

is discretized on a uniform grid:

$$\frac{\mathrm{d}u_i(t)}{\mathrm{d}t} = -\frac{\widehat{f}_{i+\frac{1}{2}} - \widehat{f}_{i-\frac{1}{2}}}{\Delta x}\,, \tag{A.2}$$

where $\widehat{f}_{i\pm\frac{1}{2}}$ are the numerical fluxes and $\Delta x = x_{i+1} - x_i$ is the uniform grid spacing. The WENO algorithm reconstructs the fluxes at the mid-points between cells $\widehat{f}_{i\pm\frac{1}{2}}$ based on the values at the center of the cells $\widehat{f}_i$.

Before applying WENO reconstruction, an upwinding direction is established using local Lax–Friedrichs flux-splitting

$$\widehat{f^{\pm}}(u) = \frac{f(u) \pm \alpha\, u}{2}\,, \quad \alpha = \max_u \left|\frac{\partial f(u)}{\partial u}\right| \tag{A.3}$$

for example. Next, the WENO reconstruction is applied to determine $\widehat{f}^{+}_{i\pm\frac{1}{2}}$ based on the point values of $\widehat{f}_i$. The main concept of the WENO method is to use a polynomial of degree k for the reconstruction, built on stencils containing $k+1$ points. For the $\widehat{f}^{+}_{i+\frac{1}{2}}$ reconstruction, the stencils (not shown here) must contain the point x_i, so that k reconstructions are formed. Next, the reconstructions are nonlinearly weighted

$$\widehat{f}^{+}_{i+\frac{1}{2}} = \sum_{r=0}^{k-1} w_r\, \widehat{f}^{(r)+}_{i+\frac{1}{2}}\,, \quad w_r = \frac{\alpha_r}{\sum_{s=0}^{k-1}\alpha_s}\,, \tag{A.4}$$

where the α_r in the construction of the weights w_r are given for example by the classical Jiang–Shu nonlinear weights [25]

$$\alpha_r = \frac{d_r}{(\epsilon+\beta_r)^2}\,, \quad \beta_r = \sum_{l=1}^{k-1}\int_{x_{i-\frac{1}{2}}}^{x_i+\frac{1}{2}} (\Delta x)^{2l-1}\left[\frac{\partial^l p_r(x)}{\partial x^l}\right]^2 \mathrm{d}x\,,$$

d_r are the optimal weights, β_r are smoothness indicators, $p_r(x)$ are the interpolating polynomials, and $\epsilon = 10^{-6}$ is a small number. The less numerically dissipative WENO-Z weights [65] are used in the simulations presented here. The construction of the weights achieves two goals:

1. in the presence of a discontinuity, the stencil that crosses the discontinuity is given an effectively zero weight, enforcing the ENO property of solutions to hyperbolic conservation laws;
2. in smooth regions, the information from the $2k-1$ points is efficiently used to give a $(2k-1)$-th order accurate solution.

A similar reconstruction is performed for $\widehat{f}^{-}_{i+\frac{1}{2}}$. Finally, the flux entering Eq. (A.2) is

$$\widehat{f}_{i+\frac{1}{2}} = \widehat{f}^{+}_{i+\frac{1}{2}} + \widehat{f}^{-}_{i+\frac{1}{2}}\,. \tag{A.5}$$

In the present simulations, a single value for the adiabatic exponent γ is specified: a multiple-γ formulation introduces nonphysical pressure oscillations near the material interfaces in conservative shock-capturing schemes for the multicomponent fluid equations [66–69]. Nonetheless, WENO schemes have been developed for two-γ formulations [51, 70].

The system of ordinary differential equations from the spatial discretization

$$\frac{\mathrm{d}u}{\mathrm{d}t} = \mathcal{L}(u,t) \tag{A.6}$$

are integrated in time using a third-order total-variation-diminishing (TVD) Runge–Kutta method [71]

$$\begin{aligned} u^{(1)} &= u^n + \mathcal{L}(u^n)\,\Delta t\,, \\ u^{(2)} &= \frac{3}{4}\,u^n + \frac{1}{4}\,u^{(1)} + \frac{1}{4}\,\mathcal{L}(u^{(1)})\,\Delta t\,, \\ u^{n+1} &= \frac{1}{3}\,u^n + \frac{2}{3}\,u^{(2)} + \frac{2}{3}\,\mathcal{L}(u^{(2)})\,\Delta t\,, \end{aligned} \tag{A.7}$$

where Δt is the timestep. These methods were developed because ordinary Runge–Kutta methods are only linearly stable and do not guarantee convergence in the presence of shocks or other discontinuities. The TVD property ensures stability of the numerical scheme [72]. In addition, a TVD scheme ensures that large oscillations are not introduced at shocks and contact discontinuities in the numerical solution.

References

[1] R. D. Richtmyer, Taylor instability in shock acceleration of compressible fluids Comm. Pure Appl. Math. 8 (1960) 297–319.

[2] E. E. Meshkov, Instability of the interface of two gases accelerated by a shock wave, Sov. Fluid Dyn. 4 (1969) 101–108.

[3] D. L. Youngs, Numerical simulation of mixing by Rayleigh-Taylor and Richt myer-Meshkov instabilities, Laser Part. Beams 12 (1994) 725–750.

[4] N. J. Zabusky, Vortex paradigm for accelerated inhomogeneous flows: Visiometrics for the Rayleigh-Taylor and Richtmyer-Meshkov environments, Ann. Rev. Fluid Mech. 31 (1999) 495–536.

[5] M. Brouillette, The Richtmyer-Meshkov instability, Ann. Rev. Fluid Mech. 34 (2002) 445–468.

[6] S. Atzeni, J. Meyer-ter Vehn, The Physics of Inertial Confinement Fusion: Beam Plasm a Interaction, Hydrodynamics, Hot Dense Matter, Vol. 125 of International Series of Monographcs on Physics, Oxford University Press, New York, 2004.

[7] G. J. Hendricks, Two Mechanisms of Vorticity Generation in Combusting F low Fields, Ph.D. thesis, California Institute of Technology (1986).

[8] D. Arnett, The role of mixing in astrophysics, Astrophys. J. Suppl. 127 (2000) 213–217.

[9] Y. Zhou, Rayleigh–Taylor and Richtmyer–Meshkov instability indu ced flow, turbulence, and mixing. I, Phys. Reports 720–722 (2017) 1–136.

[10] Y. Zhou, Rayleigh–Taylor and Richtmyer–Meshkov instability indu ced flow, turbulence, and mixing. II, Phys. Reports 723–725 (2017) 1–160.

[11] M. Latini, O. Schilling, W. S. Don, High-resolution simulations and modeling of reshocked single-mode Richtmyer-Meshkov instability: comparison to experimental data and to amplitude growth model pre dictions, Phys. Fluids 19 (2007) 024104–1–024104–24.

[12] O. Schilling, M. Latini, W. S. Don, Physics of reshock and mixing in single-mode Richtmyer-Mesh kov instability, Phys. Rev. E 76 (2007) 026319–1–026319–28.

[13] B. Thornber, J. Griffond, O. Poujade, N. Attal, H. Vãrshochi, P. Bigdelou, P. Ramaprabhu, B. Olson, J. . Greenough, Y. Zhou, O. Schilling, K. A. Garside, R. J. R. Williams, C. A. B̃atha, P. A. Kuchugov, M. E. Ladonkina, V. F. Tishkin, N. V. Zmĩtrenko, V. B. Rozanov, D. L. Youngs, Late-time growth rate, mixing, and anisotropy in the multimode na rrowband Richtmyer–Meshkov Instability: The θ-group collaboration Phys. Fluids 29 (2017) 105107–1–105107–24.

[14] B. Thornber, J. Griffond, P. Bigdelou, P. Boureima, I. a nd Ramaprabhu, O. Schilling, R. J. R. Williams, Turbulent transport and mixing in the multimode narrowband Rich tmyer-Meshkov instability, Phys. Fluids 31 (2019) 096105–1–096105–27.

[15] J. W. Jacobs, V. V. Krivets, Experiments on the late-time development of single-mode Richtmy er-Meshkov instability, Phys. Fluids 17 (2005) 034105–1–034105–10.

[16] L. D. Cloutman, M. F. Wehner, Numerical simulation of Richtmyer-Meshkov instabilities, Phys. Fluids A 4 (1992) 1821–1830.

[17] C. Pantano, R. Deiterding, D. J. Hill, D. I. Pullin, A low numerical dissipation patch-based adaptive mesh refinement method for large-eddy simulation of compressible flows, J. Comp. Phys 221 (2007) 63–87.

[18] B. J. Olson, J. A. Greenough, Comparison of two- and three-dimensional simulations of miscible Richtmyer-Meshkov instability with multimode initial conditions, Phys. Fluids 26 (2014) 101702–1–101702–7.

[19] D. Reese, C. Weber, Numerical investigation of 3D effects on a 2D-dominated shock ed mixing layer, Phys. Fluids 28 (2016) 114102–1–114102–9.

[20] A. Mosedale, D. Drikakis, Assessment of very high order of accuracy in implicit LES models, ASME J. Fluids Eng. 129 (2007) 1497–1503.

[21] V. K. Tritschler, X. Y. Hu, S. Hickel, N. A. Adams, Numerical simulation of a Richtmyer–Meshkov instability with an adaptive central-upwind sixth-order WENO scheme, Phys. Scripta T 155 (2013) 014016–1–014016–8.

[22] M. Latini, O. Schilling, W. S. Don, Effects of WENO flux reconstruction order and spatial resolutio n on reshocked two-dimensional Richtmyer-Meshkov instability, J. Comput. Phys. 221 (2007) 805–836.

[23] O. Schilling, M. Latini, High-order WENO simulations of three-dimensional reshocked R ichtmyer–Meshkov instability to late times: Dynamics, dependence on initial conditions, and co mparisons to experimental data, Acta Math. Scientia 30B (2010) 595–620.

[24] C.-W. Shu, Essentially non-oscillatory and weighted essentially non-oscillatory schemes for hyperbolic conservation laws, in: Advanced numerical approximation of nonlinear hyperbolic equations (Cetraro, 1997), Vol. 1697 of Lecture Notes in Math., Springer, Berlin, 1998, pp. 325–432.

[25] G.-S. Jiang, C.-W. Shu, Efficient implementation of weighted ENO schemes, J. Comput. Phys. 126 (1996) 202–228.

[26] D. Balsara, C.-W. Shu, Monotonicity preserving weighted essentially non-oscillatory sche mes with increasingly high order of accuracy, J. Comput. Phys. 160 (2000) 405–452.

[27] D. Drikakis, F. Grinstein, D. Youngs, On the computation of instabilities and symmetry-breaking in fluid m echanics, Prog. Aero. Sci. 41 (2005) 609–641.

[28] F. F. Grinstein, A. A. Gowardhan, J. R. Ristorcelli, Implicit large eddy simulation of shock-driven material mixing, Phil. Trans. Royal Soc. London A 371 (2013) 20120217–1–20120217–14.

[29] M. A. Jones, J. W. Jacobs, A membraneless experiment for the study of Richtmyer-Meshkov instability of a shock-accelerated gas interface, Phys. Fluids 9 (1997) 3078–3085.

[30] B. D. Collins, J. W. Jacobs, PLIF flow visualization and measurements of the Richtmyer-M eshkov instability of an air/SF_6 interface, J. Fluid Mech. 464 (2002) 113–136.

[31] O. Sadot, L. Erez, U. Alon, D. Oron, L. A. Levin, Study of nonlinear evolution of single-mode and two bubble intera ction under Richtmyer-Meshkov instability, Phys. Rev. Lett. 80 (1998) 1654–1657.

[32] B. Costa, W. S. Don, D. Gottlieb, R. Sendersky, Two-dimensional multi-domain hybrid spectral-WENO methods for conservation laws, Commun. Comput. Phys. 1 (2006) 550–576.

[33] C.-W. Shu, W.-S. Don, D. Gottlieb, O. Schilling, L. J̃ameson, Numerical convergence study of nearly incompressible, inviscid T aylor–Green vortex flow, J. Sci. Comput. 24 (2005) 1–27.

[34] M. Latini, O. Schilling, Weighted Essentially Non-Oscillatory Simulations and M odeling of Complex Hydrodynamic Flows. Part 1. Regular Shock Refr action, Tech. Rep. UCRL-TR-205132, Lawrence Livermore National Laboratory (2004).

[35] J. J. Quirk, S. Karni, On the dynamics of a shock-bubble interaction, J. Fluid Mech. 318 (1996) 129–163.

[36] K. O. Mikaelian, Growth rate of the Richtmyer-Meshkov instability at shocked i nterfaces, Phys. Rev. Lett. 71 (1993) 2903–2906.

[37] R. E. Duff, F. H. Harlow, C. W. Hirt, Effects of diffusion on interface instability between gases, Phys. Fluids 5 (1962) 417–425.

[38] R. Samtaney, N. J. Zabusky, On shock polar analysis and analytical expressions for vorticity deposition in shock-accelerated density-stratified interfaces, Phys. Fluids 5 (1993) 1285–1287.

[39] R. Samtaney, N. J. Zabusky, Circulation deposition on shock-accelerated planar and curved den sity stratified interfaces: models and scaling laws, J. Fluid Mech. 269 (1994) 45–78.

[40] Q. Zhang, S.-I. Sohn, Non-linear theory of unstable fluid mixing driven

by shock wave, Phys. Fluids 9 (1997) 1106–1124.
[41] C. Matsuoka, K. Nishihara, Y. Fukuda, Nonlinear evolution of an interface in the Richtmyer-Meshkov instability, Phys. Rev. E 67 (2003) 036301–1–036301–14.
[42] K. O. Mikaelian, Explicit expressions for the single-mode Rayleigh-Taylor and Richtmyer-Meshkov instabilities at arbitrary Atwood numbers, Phys. Rev. E 67 (2003) 026319–1–026319–7.
[43] D. Layzer, On the instability of superposed fluids in a gravitational field, Astrophys. J. 122 (1955) 1–12.
[44] V. N. Goncharov, Analytical model of nonlinear, single-mode, classical Rayleigh- Taylor instability at arbitrary Atwood numbers, Phys. Rev. Lett. 88 (2002) 134501–1–134501–4.
[45] S.-I. Sohn, Simple potential-flow model of Rayleigh-Taylor and Richtmye r-Meshkov instabilities for all density ratios, Phys. Rev. E 67 (2003) 026301–1–026301–5.
[46] S.-I. Sohn, Density dependence of a Zufiria-type model for Rayleigh-Tay lor bubble fronts, Phys. Rev. E 70 (2004) 045301–1–045301–4.
[47] J. A. Zufiria, Bubble competition in Rayleigh-Taylor instability, Phys. Fluids 31 (1988) 440–446.
[48] S.-I. Sohn, Q. Zhang, Late time behavior of bubbles at unstable interfaces in two dime nsions, Phys. Fluids 13 (2001) 3493–3495.
[49] Q. Zhang, W. Guo, Universality of finger growth in two-dimensional Rayleigh–T aylor and Richtmyer–Meshkov instabilities with all density ratios, J. Fluid Mech. 786 (2016) 47–61.
[50] L. F. Henderson, On the refraction of shock waves, J. Fluid Mech. 198 (1989) 365–386.
[51] A. Marquina, P. Mulet, A flux-split algorithm applied to conservative models for multico mponent compressible flows, J. Comput. Phys 185 (2003) 120–138.
[52] K. O. Mikaelian, Turbulent mixing generated by Rayleigh-Taylor and Richtmyer -Meshkov instabilities, Physica D 36 (1989) 343–357.
[53] K. I. Read, Experimental investigation of turbulent mixing by Rayleigh-Ta ylor instability, Physica D 12 (1984) 45–58.
[54] D. L. Youngs, Numerical simulation of turbulent mixing by Rayleigh-Taylor i nstability, Physica D 12 (1984) 32–44.
[55] M. Brouillette, B. Sturtevant, Growth induced by multiple shock waves normally incident on plane gaseous interfaces, Physica D 37 (1989) 248–263.
[56] A. A. Charakhch'yan, Reshocking at the non-linear stage of Richtmyer-Meshkov insta bility, Plasma Phys. Control. Fusion 43 (2001) 1169–1179.
[57] M. Lombardini, D. J. Hill, D. I. Pullin, D. I. . Meiron, Atwood ratio dependence of Richtmyer-Meshkov flows under resh ock conditions using large-eddy simulations, J. Fluid Mech. 670 (2011) 439–480.
[58] P. G. Saffman, D. I. Meiron, Kinetic energy generated by the incompressible Richtmyer-Meshkov instability in a continuously stratified fluid, Phys. Fluids A 1 (1989) 1767–1771.
[59] Q. Zhang, S.-I. Sohn, Quantitative theory of Richtmyer-Meshkov instability in three dimensions, Z. Angew. Math. Phys. 50 (1999) 1–46.
[60] X. L. Li, Q. Zhang, A comparative numerical analysis of the Richtmyer-Meshkov ins tability with nonlinear analysis in two and three dimensions, Phys. Fluids 9 (1997) 3069–3077.
[61] D. J. Haroldsen, D. I. Meiron, Numerical calculation of three-dimensional interfacial potential flows using the point vortex method, SIAM J. Sci. Comput. 20 (1998) 648–683.
[62] A. Majda, S. Osher, Propagation of error into regions of smoothness for accurate diff erence approximations to hyperbolic equations, Comm. Pure Appl. Math. 30 (1977) 671–705.
[63] M. Mock, P. Lax, The computation of discontinuous solutions of linear hyperbolic e quations, Comm. Pure Appl. Math. 31 (1978) 423–430.
[64] J. Casper, M. H. Carpenter, Computational considerations for the simulation of shock-induced sound, SIAM J. Sci. Comput. 22 (1998) 813–828.
[65] R. Borges, M. Ramona, B. Costa, W. S. Don, An improved weighted essentially non-oscillatory scheme for hype rbolic conservation laws, J. Comp. Phys 227 (2008) 3191–3211.
[66] S. Karni, Multicomponent flow calculations by a consistent primitive algorithm, J. Comput. Phys. 112 (1994) 31–43.
[67] S. Karni, Hybrid multifluid algorithms, SIAM J. Sci. Comput. 17 (1996) 1019–1039.
[68] R. Abgrall, How to prevent pressure oscillations in multicomponent flow calculations: a quasi-conservative approach, J. Comput. Phys. 125 (1996) 150–160.
[69] R. Abgrall, S. Karni, Computations of compressible multifluids, J. Comput. Phys 169 (2001) 594–623.
[70] D. J. Hill, D. I. Pullin, Hybrid tuned center-difference-WENO method for large eddy simul ations in the presence of strong shocks, J. Comput. Phys. 194 (2004) 435–450.
[71] C.-W. Shu, S. Osher, Efficient implementation of essentially nonoscillatory shock-capturing schemes, J. Comput. Phys. 77 (1988) 439–471.
[72] A. Harten, High resolution schemes for hyperbolic conservation laws, J. Comput. Phys. 49 (1983) 357–393.